Efficient Gas Separation and Transport Mechanism in Rare Hemilabile Metal-Organic Framework

Marta Mon,[†,◊] Rosaria Bruno,[♣,◊] Estefanía Tiburcio,[†] Aida Grau-Atienza,[§] Antonio Sepúlveda-Escribano,[§] Enrique V. Ramos-Fernandez,[§] Alessio Fuoco,[‡] Elisa Esposito,[‡] Marcello Monteleone,[‡] Johannes C. Jansen,[‡] Joan Cano,[†] Jesús Ferrando-Soria,*[,†] Donatella Armentano*[,♣] and Emilio Pardo*[,†]

[†]Instituto de Ciencia Molecular (ICMol), Universidad de Valencia, 46980 Paterna, Valencia, Spain

[§]Laboratorio de Materiales Avanzados, Departamento de Química Inorgánica-Instituto Universitario de Materiales, Universidad de Alicante, Alicante, Spain.

[‡]Institute on Membrane Technology, ITM-CNR, Via P. Bucci 17/C, 87036 Rende, Italy.

[♣]Dipartimento di Chimica e Tecnologie Chimiche (CTC), Università della Calabria, Rende 87036, Cosenza, Italy

◊These authors equally contributed to the work.

ABSTRACT: Understand/visualize the established interactions between gases and adsorbents is mandatory to implement better performant materials in adsorption/separation processes. Here we report the unique behavior of a rare example of a hemilabile chiral three-dimensional metal-organic framework (MOF) with an unprecedented **qtz-e**-type topology, with formula Cu^{II}_2(S,S)-hismox · $5H_2O$ (**1**) (hismox = bis[(*S*)-histidine]oxalyl diamide). **1** exhibits a continuous and reversible breathing behavior, based on the hemilability of carboxylate groups from L-histidine. In-situ powder (PXRD) and single crystal X-ray diffraction (SCXRD) using synchrotron radiation allowed to unveil the crystal structures of 4 different host-guest adsorbates (**Ar**, **N_2**, **CO_2** and **C_3H_6@1**), the rationalization of the breathing motion and unravel the mechanisms governing the adsorption of these gases. Then, this information has been transferred to implement efficient separations of mixtures of industrial and environmental relevance –CO_2/N_2, CO_2/CH_4 and C_3H_8/C_3H_6 using **1** in packed columns as the stationary phase and dispersed in a mixed matrix membrane.

INTRODUCTION

Metal–organic frameworks[1–4] (MOFs) are solid crystalline porous materials that have been extensively studied in last decades, due to the myriad of useful and exploitable properties that they can exhibit, such as gas adsorption[5] and separation,[6] catalysis,[7–10] magnetism,[11] conductivity[12] and water harvesting.[13] Among them, gas adsorption/separation processes have traditionally captured most attention due to their intrinsic porous nature and the possibility to fine-tune, pre- or postsynthetically,[14,15] such porosity in terms of size, shape and/or functionality of the MOFs channels, in order to modify adsorption affinities and/or separation capabilities.[16] In addition, the unique stimuli-responsive flexibility[7,17] and adaptability[18] of some MOFs can also account for the selectivity observed in the separation of specific molecules.[19]

The resolution of the crystal structure of the host-guest adsorbate[20–22] is the most effective and direct way to visualize and rationalize these adsorption mechanisms. However, the number of reports showing these crystal structures is still limited and most of them have been resolved by powder X–ray diffraction[23–26] (PXRD) and neutron powder diffraction[27–34] (NPD) methods. Even fewer crystal structures were resolved by single crystal X–ray diffraction[35–50] (SCXRD) – which offers unambiguous results with much more precise structural parameters – and these were focused mainly on CO_2-adsorbed materials.

Among the total MOFs reported in literature, only a select group of MOFs have network flexibility and exhibit breathing, under application of external stimuli.[51,52] This phenomenon is directly related to stepped adsorption isotherms, which may lead to hysteretic adsorption behavior with great potential impact on the gas separation properties.[53]

In this work, we report a novel very robust and flexible water-stable microporous three-dimensional (3D) MOF (Figure 1a), prepared with an oxamidate ligand[15,54–60] derived from the natural amino acid *L*-histidine (Figure 1b), of formula Cu^{II}_2(*S,S*)-hismox · $5H_2O$ (**1**) (where hismox[15] = bis[(*S*)-histidine]oxalyl diamide). The present material features intricate and narrow distorted triangular channels, which are decorated with a number of accessible Cu(II) sites and aromatic imidazole rings from the amino acid residue histidine (Figures 1c-d). This material exhibits great robustness but also a singular flexible network –due to the presence of specific temperature– and adsorbate-responsive structural features, which can induce a reversible and continuous breathing of the MOF. This phenomenon is visualized by means of SC-XRD of **1,** which constitutes one of the very few examples showing such continuous breathing, along with MIL-88[61,62] and SHF-61[53]. It finally experiences a gas-driven phase transition without change in crystalline

phase at low pressures, from a stable guest-free phase to give a larger-pores phase, which is reflected in two-step adsorption isotherms. The extremely high crystallinity and robustness of **1** allowed the resolution of the crystal structures of 4 different host-guest adsorbates (Ar, N_2, CO_2 and C_3H_6) by means of SC-XRD. This offered unprecedented snapshots on the mechanisms governing the adsorption of these gases and the subsequent impact on its separation properties. Separation of some common mixtures of gases is of main relevance in industrial chemical processes. These separations include the selective capture of greenhouse gases – like CO_2 or CH_4 – or the separation of different mixtures of hydrocarbons; amongst which olefin/paraffin separations stand out.[63] Current separation methods consume large amounts of energy and resources. Thus, the development of new materials with improved separation properties will have a major impact on society from both environmental and economic view-points.[64] To this end, it is crucial to understand the host-guest interactions operating in the gas adsorption/separation processes. In particular, **1** carries out efficiently the kinetic separation of mixtures of CO_2/N_2, CO_2/CH_4 and C_3H_8/C_3H_6.

RESULTS AND DISCUSSION

Preparation and X-ray Crystal Structure. Compound **1** is obtained at large scale by decreasing the pH of an aqueous $(Bu_4N)_2\{Cu_2[(S,S)\text{-hismox}](OH)_2\} \cdot 4H_2O$ solution to pH = 4 with diluted HCl. In addition, at small scale, a slow diffusion technique yields larger blue rectangular prisms suitable for X-ray diffraction (see Supporting Information for details).

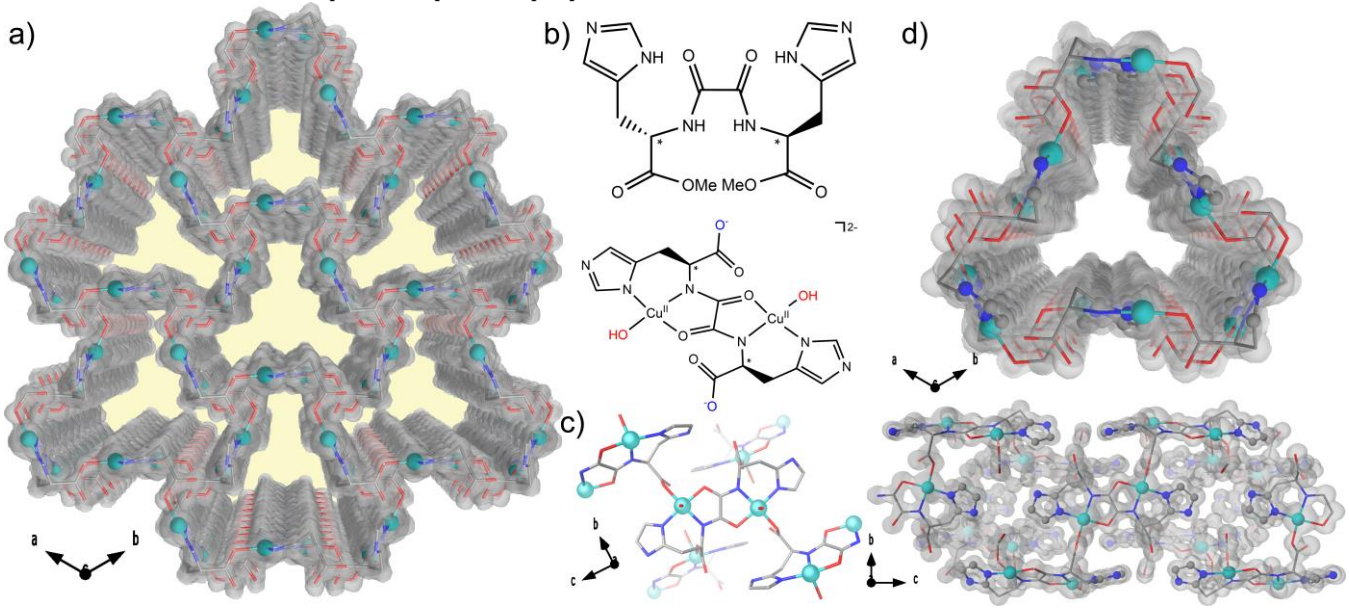

Figure 1. (a) Perspective view of the 3D open-framework of **1** (110 K) along the *c* axis (the crystallization water molecules are omitted for clarity). (b) Chemical structures of the chiral bis[(*S*)-histidine]oxalyl diamide ligand (top) and the corresponding dianionic bis(hydroxo) dicopper(II) complex (bottom), highlighting the potential coordination sites (blue and red) and the chiral centers (*). (c) Perspective view of a fragment of **1** in the *bc* plane, showing the dinuclear units coordination modes. (d) Perspective views of one single channel of **1** in the *ab* (top) and *bc* (bottom) planes. The ligands are depicted as sticks and the copper(II) cations as spheres, both with surfaces. In d, C and N atoms constituting the imidazole rings are shown using the spheres and sticks mode. Color codes: Cu: cyan; O: red; C: gray; N: blue.

Crystal structure of the MOF. 1 The structures of **1** in the 110-350 K range of temperature and ambient pressure were solved with single-crystal X-ray diffraction at the Synchrotron Light Source, Diamond, UK (Figure S1, Table S1).

Analysis of the structure of **1** at 110 K (Figure 1) shows that the material crystallizes in the hexagonal space group $P3_121$ with unit cell dimensions $a = 10.5763$ (12) Å and $c = 16.8289$ (6) Å, and has the unique **qtz-e**-type topology (Figure S2) with no occurrence in MOFs' topologies database.[65] The framework comprises six connecting nodes of *trans*-oxamidato-bridged dicopper(II) units, $\{Cu^{II}_2[(S,S)\text{-hismox}]\}$ (Figure 1b), bridged by the carboxylate of the histidine moieties acting as monodentate linkers, creating an infinite chiral porous 3D framework (Figure 1c). Coordinated water molecules occupy the apical site on each of the Cu centres and form strong hydrogen bonds [O···O and H···O-H of 2.45(1) and 1.63(3) Å, respectively] with crystallization water molecules. Free imidazole N atoms on $\{Cu^{II}_2[(S,S)\text{-hismox}]\}$ units are involved in hydrogen bonds with -O–CO groups of the histidine residues occupying adjacent sheets [O···N and O···H-N of 2.756(3) and 2.03(3) Å, respectively]. The weak interaction of this imidazole···carboxylate is a key intrinsic feature, as it is at the origin of its hemilability. It is retained by the net, being still very active and dynamic as well, in the dehydrated phase of **1** (*vide infra*). All Cu centres are crystallographically equivalent, exhibiting a square-pyramidal ($CuN_2O_2O_{water}$) geometry (Figure 1c). The five-coordinated Cu metal centres have different Cu–O and Cu-N bond lengths for the basal/equatorial planes [1.95(1)–1.97(1) Å] and the apical ones [2.483(1) Å]. The **qtz-e** lattice has one type of unidimensional trapezoidal nanosized channels growing along the [001] direction (Figures 1a and 1d), with effective calculated void volumes, at 110 K, of 30.5% [total potential accessible volume of 497.9 $Å^3$ of 1629.9 $Å^3$

of the unit cell]. The channels contain both coordinated and lattice water molecules.

PXRD and TGA experiments. The powder X-ray diffraction (PXRD) pattern of a polycrystalline sample of **1** (Figure S3) fits perfectly with the calculated pattern (Figure S3a), which confirms the purity of 1 and the isostructurality of the bulk with the crystals selected for single crystal X-ray diffraction. The water content of 1 was established by thermogravimetric analysis under dry N_2 atmosphere (TGA, Figure S4) and elemental CHN analyses (Experimental section at SI). Figure S4 shows a fast mass loss from room temperature, followed by a *plateau* in the range of 95-280 °C, where decomposition starts. The weight loss of 16.2% at 150 °C closely corresponds to 5 water molecules.

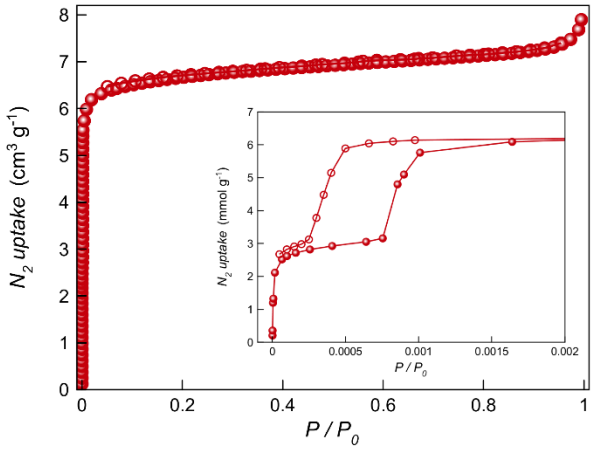

Figure 2. N_2 (77 K) adsorption isotherm for the activated compound **1**. Filled and empty symbols indicate the adsorption and desorption isotherms, respectively. The inset shows the two-step gas adsorption and the hysteresis in the desorption process at low pressures.

Gas adsorption experiments. Compound **1** was activated, prior to the sorption measurements, by soaking the sample in methanol for 60 min, followed by drying under reduced pressure for 24 h at 80 °C. The N_2 adsorption isotherm at 77 K (Figure 2) shows a type I isotherm, characteristic of microporous materials with permanent microporosity, with an estimated Brunauer–Emmett–Teller (BET) surface area[66] of 624 $m^2 g^{-1}$. Interestingly, the N_2 sorption isotherm exhibits a two-step hysteresis (inset of Figure 2). The first step, which occurs at very low-pressures ($P = 2.0x10^{-6}$–$2.8x10^{-4}$ bar), fits well with the adsorption of *ca.* 3 mmol of N_2 per formula unit. The sharp second step corresponds to the adsorption of 3 more mmol of N_2 per formula unit ($P = 1.1x10^{-3}$–$1.7x10^{-3}$ bar) to reach a "pseudo-plateau" that increases smoothly to reach a saturation value of *ca.* 7 mmol of N_2 per formula unit.

Interestingly, very similar behaviour is observed for the Ar (77 K) and CO_2 (195 K and 273 K) adsorption isotherms (Figures S5 and S6) with a two-step adsorption of *ca.* 3 and 6 mmol of Ar and 1.5 and 3 mmol of CO_2 per formula unit. Overall, such two-step hysteretic adsorption behaviour for N_2, Ar and CO_2 can be attributed to both framework flexibility and/or a gas molecules relocation.

Synchrotron powder X-ray diffraction. *In-situ* Synchrotron Powder X-ray Diffraction (S-PXRD) measurements of **1** at different temperatures and in the presence of different gases unveiled the origin of this two-step adsorption and to elucidate the gas adsorption interactions.

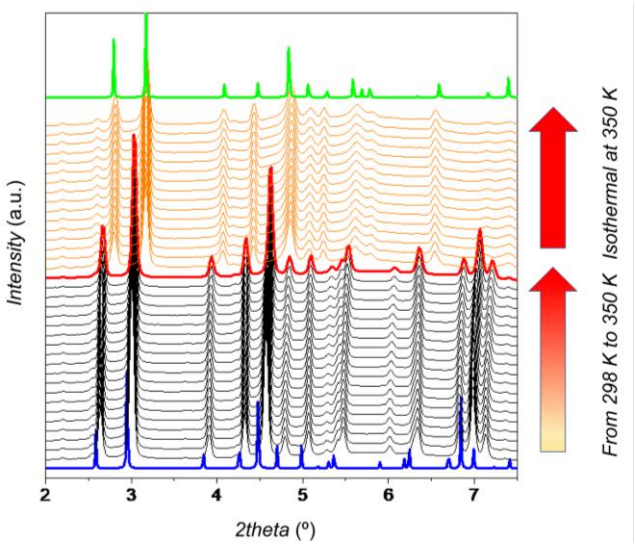

Figure 3. S-PXRD experiments for compound **1** at different temperatures and under vacuum. From the bottom to the top: pattern of simulated hydrated phase (blue), *T*-dependent S-PXRD patterns in the 298-340 K range (black), S-PXRD patterns at 350 K within 30 min. (orange), simulated pattern of the dehydrated phase (green). Solid red line represents the last spectra before the phase transition.

The diffraction pattern of the sample was monitored during activation under vacuum from 298 K to 350 K and only shows a sudden shift of nearly all peaks to higher angles around 250°C, after which it remains constant. The S-PXRD pattern of **1** at different temperatures, showing this dramatic change in the crystal structure, indicate that **1** is sensitive to the desolvation, but once it is dehydrated, the structure remains unaltered. Exposure of the activated sample to air showed complete reversibility of the process.

Isobaric experiments with N_2, Ar, CO_2 and C_3H_6 at 5 bar accomplished saturation of activated **1** upon cooling from 350°C (Figures S7-S10). The structure of **1** behaves very similar upon adsorption of the different gases. Thus, once the sample is pressurized with the gases at high temperature (350 K), the diffraction pattern shifts towards lower *2 theta,* indicating that when a small amount of gas is adsorbed, the structure of **1** starts assuming an analogous structure as the hydrated one. Interestingly, this happens for all gases, including Ar and N_2, which are very far from the condensation point (see phase diagram, Figures S7-S10). These results suggest that the structure of **1** is extremely sensitive to gas adsorption and, when the first molecules of an adsorbate enter the pores, the structure of the sample changes. However, the same structure of the fully hydrated MOF was not achieved with any of the gases, showing that the interaction of the framework with permanent gases is weaker than that with water vapor.

Overall, S-PXRD experiments confirm that the framework is highly flexible and that the (de)hydration of the sample produces a pronounced and reversible change in the structure, while gases have a similar but less pronounced effect, depending on their polarity, size and shape. Nevertheless, S-PXRD does not allow to identify which specific interactions

of the different gases with the framework are responsible for the breathing.

Crystal Structures of the activated and gas-adsorbed phases. *In-situ* SC-XRD experiments with synchrotron radiation on a single crystal of **1** in the presence of different gases (N_2, Ar, CO_2 and C_3H_6) at variable temperature and pressure, yielded much more detailed information (Figures 4-6) than the powder experiments. The temperature increase of **1** induces a delicate breathing motion of its crystal structures, culminating in a sudden contraction of the cell volume at high temperatures and under vacuum (Figures 4 and S12-S14 and Tables S1-S3 and video S1). A slightly positive thermal expansion (PTE) over the temperature range of 110-290 K is followed by an abrupt contraction of the a and c axes (see Figure S13 and Tables S1-S2) and lower volume at 320 K and 350 K (Table S2 and Figure S12). The large breathing motion is associated with the removal of the water molecules (Figure 4) accounting for a large decrease in the unit-cell volume (total $\Delta V \approx 325$ Å^3, ~22%, Table S2 and Figure S12).

Noteworthy, the deformation of the framework during the breathing process is not accompanied, by a crystalline phase transition. The dehydrated phases (Figure 4) maintain symmetry and still exists in the $P3_121$ space group. The structural changes are most evident in the crystallographic *a*- and *c*-axis directions showing strong contractions ($\Delta a \approx -0.81$ Å and $\Delta c \approx -0.84$ Å, see Table S2) over the range of breathing motion. The dehydrated network is stable and does not show strong further changes upon heating (see **1@320K** and **1@350K**, Table S2) or upon cooling of the dehydrated **1** in 250-110 K range of temperatures (Table S3). The whole process gives rise to two main distortions of the framework: (*i*) an important motion of each carboxylate group of the histidine moiety towards the Cu centers that assists the change in the coordination environment of the copper metal ions –hemilability– (Figures 5 and S11), which results in a narrowing of the trapezoidal channels in the *ab* plane (Figure 4); and (*ii*) a compression of the copper chiral chains along the *c* channel direction, for which the length of the axis is reduced. (Figures 5 and 6). Noteworthy, the main contributor to the breathing mechanism in **1** –the change in copper coordination sphere (hemilability, Figure 5)– is totally different to that of other MOFs exhibiting breathing behavior, such as MIL-53, MIL-88 and DMOF,[67] for which the ligand hinge motion accounts for the breathing behavior.

Upon heating to 350 K, **1** undergoes a single-crystal-to-single-crystal transition (Table S2), which reverses upon exposure to air at 298 K (Table S4). The unit cell changes at 350 K to 10.055(3) Å and 16.302(6) Å for *a* and *c,* respectively (see Figure 4 and Table S1 for fully solvated unit-cell parameters). Figures 4 and 6 show loss of both free and coordinated water molecules, while the frameworks are still composed of one crystallographically unique Cu centre and one unique hismox ligand with empty trapezoidal channels.

Dehydration deforms the unique **qtz-e** net (Table S3). Coordination sites that were previously occupied by coordinated water molecules (Cu–O distance = 2.483(2) Å) are then occupied by μ_2-coordinated carboxylate O atoms (Cu–O, 2.670(2) Å or 2.626(3) Å at 320 K and 350 K, respectively) from neighboring *trans* oxamidato-bridged dicopper(II) units, {Cu^{II}_2[(S,S)-hismox]} (Figures 5 and 6). The latter are still H-bonded to free –NH groups of imidazole and their H-bond acts as a pivot for O-CO motion (Figure S11). Thus, during the evacuation process, a significant oscillation of carboxylate groups, H-bond assisted, move them from a Cu···O distance greater than 3.0 Å [3.014(3) Å for 110 K crystal structure] to the lower values reported above, revealing an established bond with copper metal ions (hemilability). This change in coordination environment of the Cu centers does not alter the dimensionality of the framework but triggers the breathing affecting the dimension of the channels. The combined structural variation and the new conformation arrangement results in a large decrease of the Cu···Cu [from 8.442 to 7.771 Å] and O···O [from 6.779 to 6.083 Å] separations of each *waving* carboxylate O atoms on neighbouring {Cu^{II}_2[(S,S)-hismox]} dimers within narrow window of each pore (Figures 5, 6 and S11).

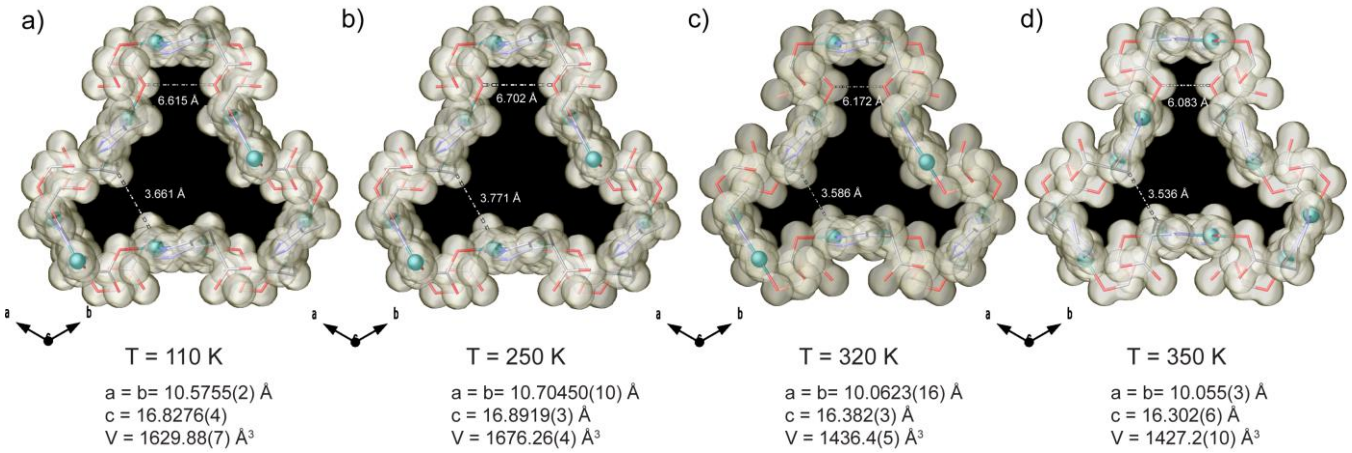

Figure 4. View of one single channel of **1** in the *ab* plane for selected temperatures: 110 K (a), 250 K (b), 320 K (c) and 350 K (d) (the crystallization water molecules are omitted for clarity) with most relevant structural parameters. The ligands are depicted as sticks and the copper(II) cations as spheres, both with surfaces. Color codes: Cu: cyan; O: red; C: gray; N: blue.

Interestingly, during the evacuation process, it has been possible to take a snapshot of the *transient* adopted by the net before getting the most stable dehydrated conformation (Figure 6). Surprisingly, the transient is the most 'open' crystal structure. This unique transient only occurs in the freshly activated MOF and does not re-appear after cooling

and heating to the same temperature. Our hypothesis is that the loss of water imposes a first *transient* step in response to the change in the coordination number from five to four, in which the new geometry around the Cu centers imposes first only a flattening of the basal plane, still reminiscent of the hydrated network, with a consequent increase of the bond lengths in copper environment. (Figure S11b, left). Then, the flexible -O–CO groups rotate to bind sites that were occupied by the water molecules, rather than leaving these sites vacant. On exposure to humidity from air, **1** quickly reverts to the original as-synthesized crystal structure (Table S4). On the other hand, synchrotron powder X-ray diffraction did not show any evidence of the *transient* structure (Figures 6 and S11), which suggest that such 'transient' shift occurs faster or in a less collective fashion in the dehydration of powders, where different size and shape of crystallite contributions may quench the bulk effect. As far as we know a such unambiguous visualization of a complete rearrangement process of a MOF single crystal upon dehydration, showing the occurrence of diverse steps before pore's contraction, is unprecedented in a MOF.

The origin of robustness, reversibility and hydrolytic stability of **1** and few other hemilabile MOFs[68] is connected with the presence of coordinated solvent molecules that may be removed by heating and/or under vacuum, leaving open metal sites within the MOF pores, which interact with new guest molecules. The weak coordination interactions involving carboxylate groups attenuate the coordination change effect. On rehydration, these weak bonds are broken and the framework returns to its original hydrated form (Figure 5). The energy released by the adsorption of water molecules is used to break these long Cu–O bonds, rather than Cu–O bonds in network that hold the framework together (Figures 1c and S11).

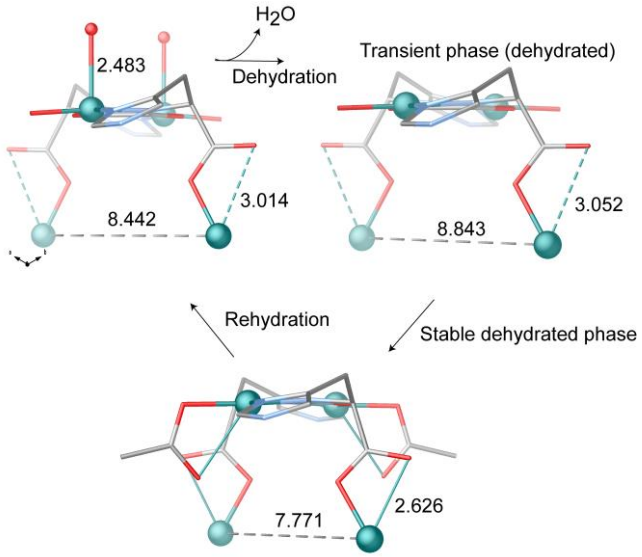

Figure 5. View of a fragment of **1** emphasizing the changes in the copper(II) environment during the reversible breathing process [Structural parameters are reported in Å].

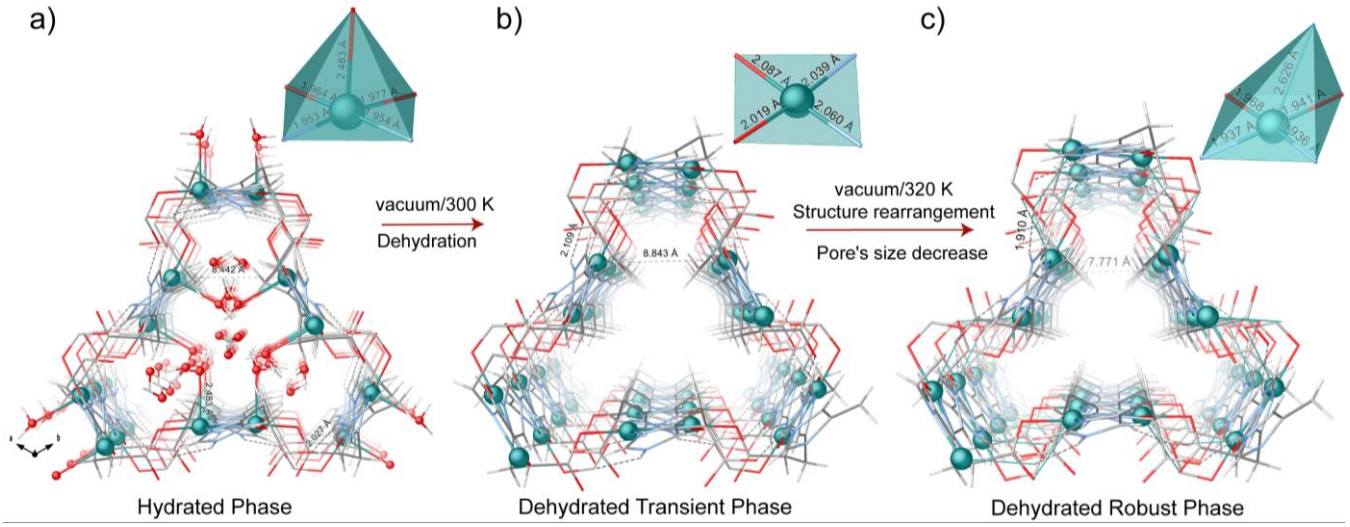

Figure 6. (a) View along the *c* axis of one pore's details of the 3D open-framework from original structure of **1** (at 110 K, the guest water molecules are represented as red spheres whereas hydrogen as with sticks) through evacuation process generating *transient* (b) and then robust dehydrated phases (c) where a significant conformational rearrangement occurred. The main structural variations are shown in detail (dashed lines). Color codes: Cu: cyan; O: red; C: gray; N: blue.

The direct structural characterization of N_2, Ar, CO_2 and C_3H_6 adsorption in single crystals of **1** (Figures 7 and S15-S20 and Table S5) under rigorously air-free conditions confirms that a larger-pores phase is reobtained after exposing the stable guest-free phase to the gases, in agreement with S-PXRD (Table S5). Furthermore, each gas, except Ar (Figure S17), interacts with the exposed copper(II) site (Figures S15-S20) and this allows the identification of secondary (for N_2, and CO_2) and tertiary (for N_2) adsorption sites (Figures S15 and S18, respectively) within the framework. Remarkably, further inspection of Cu^{II}–gas distances reveals that binding occurs primarily through both strong (for N_2, CO_2 and C_3H_6) and weak (for N_2, Ar, CO_2 and C_3H_6) interactions (see Single Crystal X-ray Diffraction section at the Supporting Information for an in depth analysis of **N_2@1**, **CO_2@1**and **Ar@1** crystal structures). The total amount of gas molecules detected by *in-situ* SC-XRD experiments fits well with that observed in the gas adsorption measurement, except for Ar.

Inspection of the {Cu_2[(*S,S*)-hismox]}·0.66Ar structure shows no direct bond between Ar and the framework, as expected for such a symmetric atom without quadrupole moment capable to interact with the dipole moment of the metals. This point must be responsible for the lower Ar loading in the structure compared to N_2, CO_2 and C_3H_6 adsorbates and gas-sorption measurements. The higher disorder of these *free* atoms, probably does not allow to define all Ar atoms. The Cu–C_3H_6 interactions observed in **1** represent, to the best of our knowledge, the first single-crystal structure determination of a metal–C_3H_6 interaction, which were so far only determined by neutron powder diffraction (NPD).[28,30,34]

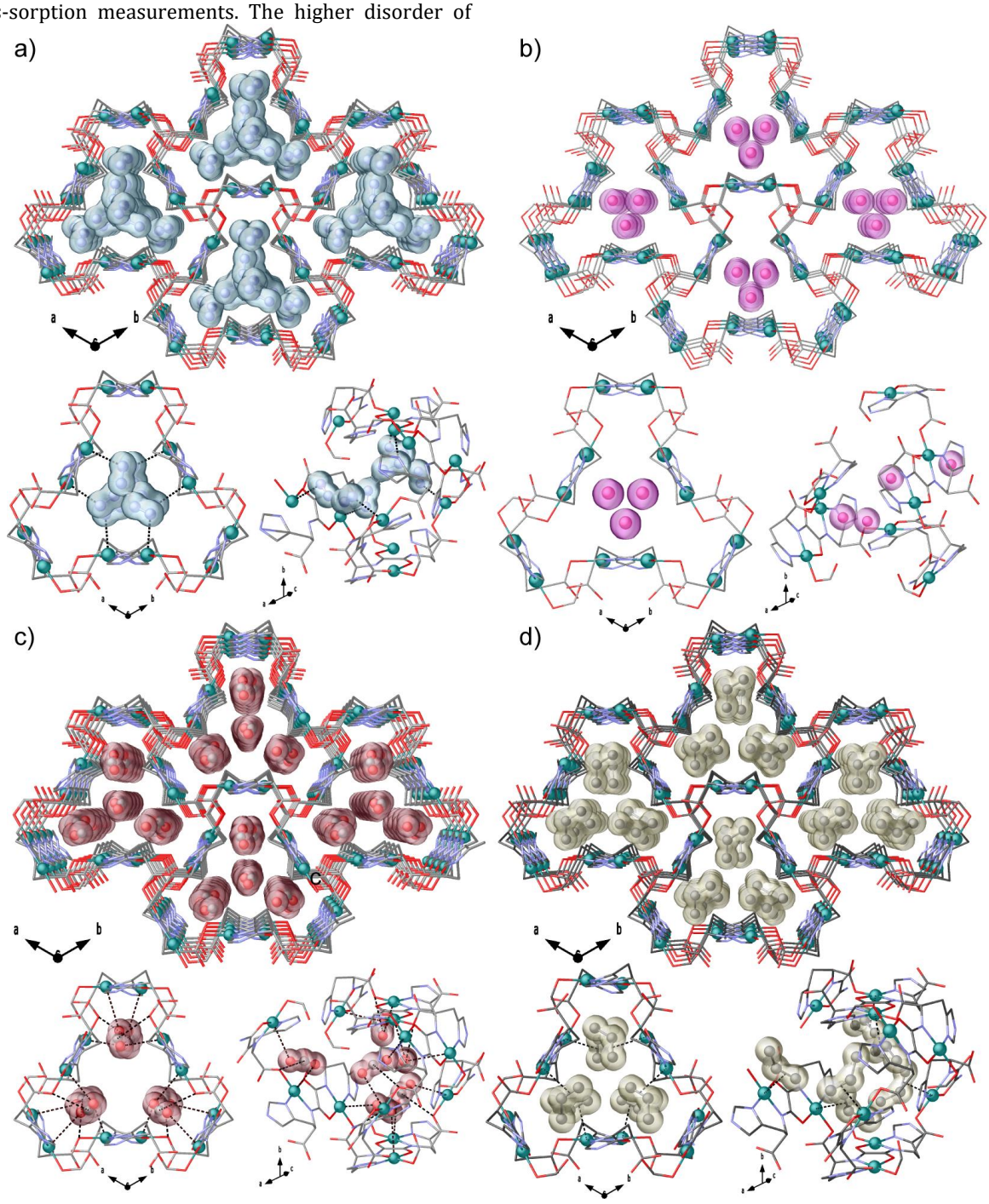

Figure 7. Perspective views of the porous structures determined by single-crystal X-ray diffraction of the host-guest adsorbates containing N_2 (a, 110 K and 7. 4 bar), Ar (b, 120 K and 10 bar), CO_2 (c, 235 K and 9.4 bar) and C_3H_6 (d, 290 K and 7.5 bar). Copper(II) atoms are depicted as spheres and sticks whereas ligands are represented as sticks. The guest gases are represented as spheres and sticks with surfaces. The host-guest interactions are shown in detail (dashed lines) in the right side of the porous structures. Color codes: Cu: cyan; O: red; C: gray; N: blue.

The X-ray analysis of a single crystal of **1** under 7.5 bar of C_3H_6 at 290 K resulted in the {Cu_2[(*S,S*)-hismox]} · 2C_3H_6 crystal structure (Figures 7d, S20 and S21). Noteworthy, below 1 bar of C_3H_6 at 230 K, the structure showed no

marked subnetwork displacements, indicative of a high affinity of the net for the gas as shown by gas adsorption isotherms. A direct bond involving the unsaturated carbon-carbon bond of the C_3H_6 molecule and Cu(II) ions can be observed at 2.33 Å and 2.61 Å, for 7.5 bar/290 K and 1 bar/230 K, respectively. This is the shortest distance among the studied gases (Figures S20 and S21), and further supports the presence of strong network-gas interactions. In both the low and the high pressure regime, C_3H_6 preferentially forms single C_3H_6···Cu(II) adducts with this unique adsorption site, and the guest molecules are never confined at the center of the channels but interact weakly with the pore wall (Figure 7d).

Breakthrough experiments. Adsorption isotherms for the hydrocarbons methane (CH_4), propane (C_3H_8) and propylene (C_3H_6), and for N_2 and CO_2 at 298 K (Figure S22), indicate that only CO_2, C_3H_8 and C_3H_6 are adsorbed significantly, whereas CH_4 and N_2 are virtually not adsorbed. These results suggest potentially high theoretical selectivities for the separation of N_2/CO_2 and CH_4/CO_2 gas mixtures and also a moderate theoretical C_3H_8/C_3H_6 selectivity that increases under kinetic conditions (breakthrough experiments, *vide infra*). This can be attributed to the higher interactions between C_3H_6 and the framework, as determined by SC-XRD.

Breakthrough experiments[69] in packed columns of **1** as the stationary phase (Figure 8) show that the N_2/CO_2 and CH_4/CO_2 separations are fully achieved, whereas N_2 and CH_4 break at the same time as H_2, indicating no N_2 and CH_4 adsorption. However, CO_2 is adsorbed for a duration of *ca.* 13.5 min., which corresponds to the maximum adsorption capacity of ~34 $cm^3\ g^{-1}$ of **1** at 298 K, and indicates that selectivity for this separation is extremely high. For the C_3H_8/C_3H_6 mixture (Figure 8c), C_3H_8 breaks 3 min later than H_2 and C_3H_6 breaks 7.5 min after C_3H_8, indicating a maximum total adsorption of ~15 $cm^3\ g^{-1}$ and 47.5 $cm^3\ g^{-1}$, respectively. This is in agreement with the much higher affinity of **1** for C_3H_6 then for C_3H_8 adsorption (Figure S22). This scenario with a central role of the metal center may be at the origin of selective behavior of **1**.

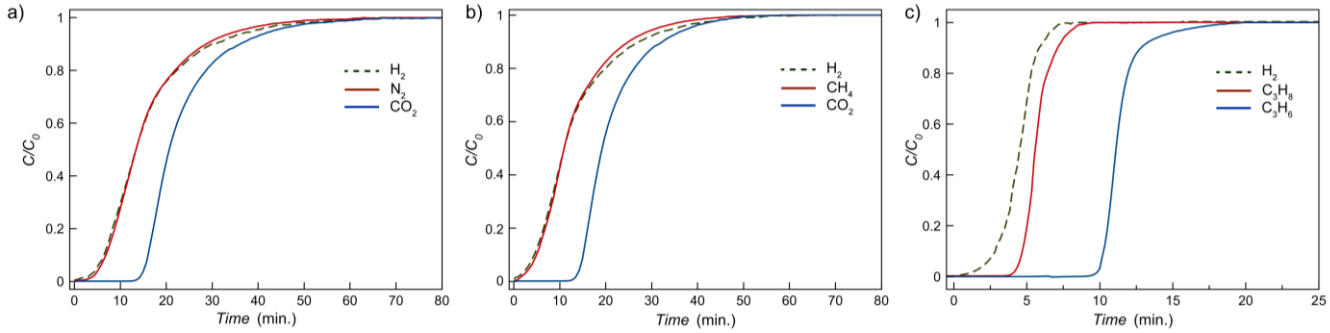

Figure 8. Experimental column breakthrough curves for N_2/CO_2 (75:25, v/v, (a)), CH_4/CO_2 (75:25, v/v, (b)) and C_3H_6/C_3H_8 (50:50, v/v, (c)) gas mixtures measured at 298 K and 1 bar in a column using 1 (*ca.* 1 g) as stationary phase. The total flow was 12 mL min^{-1}. H_2 was used as reference gas.

Mixed matrix membranes based on Pebax1657®/1 for gas separation. MOF **1** is an appealing candidate for the fabrication of membranes, useful for gas application, due to its remarkable CO_2 adsorption capacity as well as its selectivity. As a further confirmation, **1** was dispersed in a film of the poly(ether-co-amide) multi-block copolymer Pebax®1657 in order to obtain a defect-free mixed matrix membrane with homogenous dispersion of **1** (Figure 9). This is a model system for mixed matrix membranes, currently at the center of the attention for gas and vapor separation applications.[70,71]

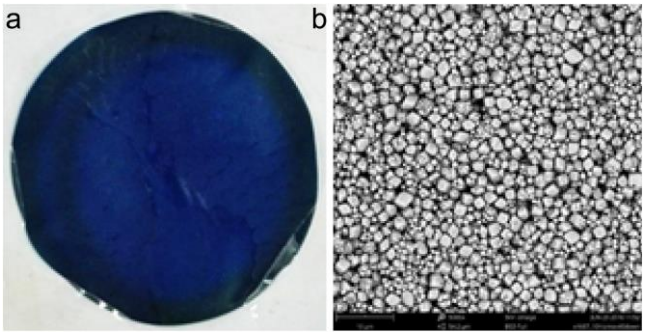

Figure 9. (a) Photograph of a representative Pebax®1657/**1** mixed matrix membrane. (b) SEM image of MMMs with a loading of 22 vol% of **1**.

The advantage of Pebax®1657 is that it does not affect the overall permeability for the gases of interest (Figure 10a), which makes it ideally suitable for the study of transient phenomena. Gas permeability measurements were carried out with pure gases by a standard time lag instrument and with gas mixtures by an innovative setup with on-line mass spectrometric analysis of the gas composition.[72] Details of the permeability measurements are given in the Supporting Information. In contrast to the constant permeability, there is a remarkable decrease of the effective pure gas diffusion coefficient with increasing MOF content (Figure 10b). Details of the permeability measurements are given in the Supporting Information. In contrast to the constant permeability, there is a remarkable decrease of the effective pure gas diffusion coefficient with increasing MOF content (Figure 10b).

Given the well-known equation describing the solution-diffusion mechanism, P = D x S (where P = permeability, D = diffusion coefficient and S = gas solubility), a reduction in the diffusion coefficient and constant permeability means a corresponding increase in the gas solubility (Figure 10c), in agreement with the high sorption capacity of **1** discussed above. The strong CO_2-**1** interaction was confirmed by the anomalous trend in the diffusion coefficient for CO_2 as a function of the feed pressure monitored in the range 0.1-1.5 bar for the Pebax®1657/22 vol% MOF **1** MMMs (Figure

S23). The anomaly originates from the high affinity of CO_2 for **1** which, affects negatively the diffusion coefficient at low feed pressure, boosting at the same time the solubility. The sorption isotherms of the six gases, determined from the indirectly calculated solubility ($C=S \times p_{feed}$), show a clear dual mode sorption behavior for CO_2, and a greater affinity of CO_2 with MMMs with respect to the other gases (Figure S24). The characteristic gas interaction properties of **1** were further confirmed under mixed gas conditions. The membrane Pebax®1657/**1** with 22 vol% of MOF **1** was tested using two binary mixtures CO_2/CH_4 (35/65 v/v) and CO_2/N_2 (85/15 v/v). Figure 11a shows the typical sigmoidal curve of CO_2 permeate flow rate during single and mixed gas permeation, in the presence of N_2 and CH_4 for CO_2/N_2 and CO_2/CH_4 binary mixtures, respectively. The permeation of CO_2 slows down markedly by the presence of methane and nitrogen. This behavior was not observed for the neat Pebax® membrane (Figure 11b) confirming the strong CO_2–**1** interaction. For a more accurate analysis of the transient behavior, the permeate flow rate curves of the two binary mixtures were fitted with Eq. S1 (Figure S25) describing Fickian diffusion in nonporous polymers. The high precision fit strongly underestimates the early stage of the methane and nitrogen permeation curves. This very fast transient behavior is associated to the preferential penetrant transport in non-interacting channels formed by compound **1** cavities, confirming the poor adsorption anticipated by the breakthrough curves. Instead, the CO_2 transient permeation is somewhat slower than the theoretical curve, indicating the existence of a stronger CO_2-membrane interaction in this Pebax®1657/**1** MMM with respect to that in the neat polymer.

This strong interaction makes this innovative material a good candidate for the potential design and development of mixed matrix membranes or even membrane reactors, where the separation properties of the membrane can be coupled with the presence of a catalyst in the MOF.

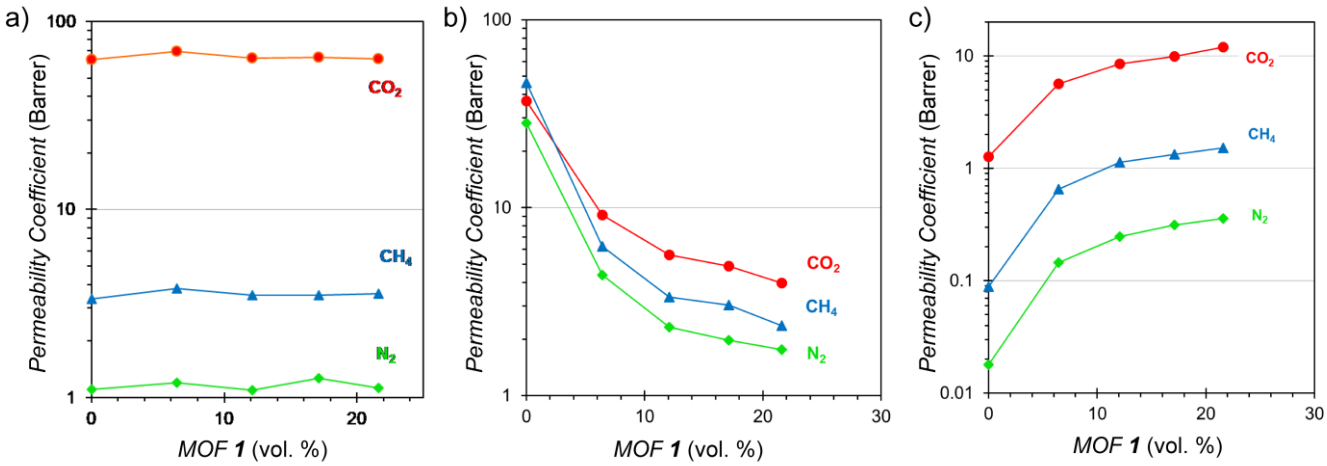

Figure 10. Single gas permeability (a), diffusion (b) and solubility (c) coefficients for CO_2, CH_4 and N_2 of **1** loaded in Pebax®1657 as function of the MOF concentration.

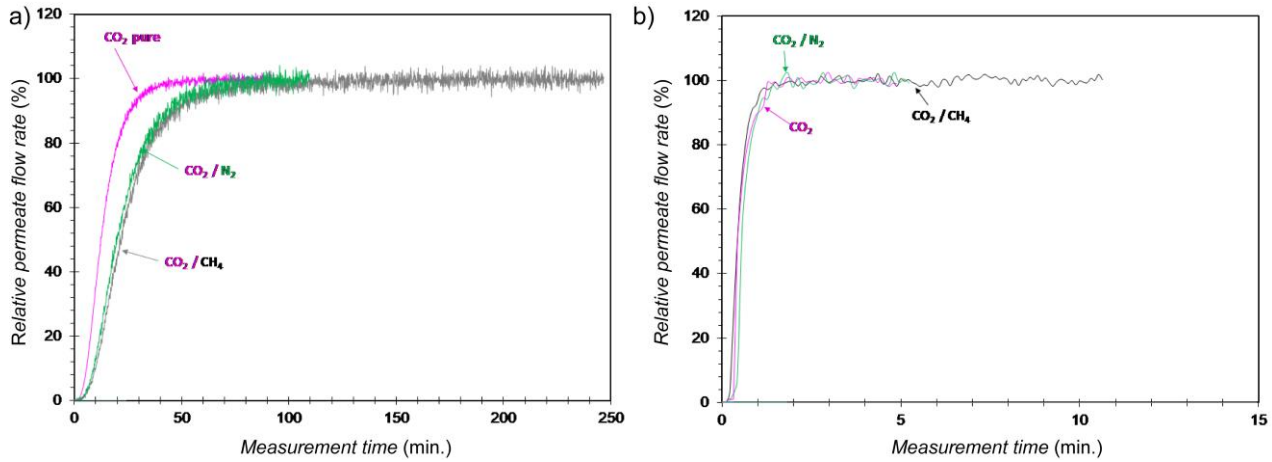

Figure 11. Comparison of Sigmoidal curve of CO_2 permeate flow rate for MMMs based on Pebax1657/**1** (a) and for pure Pebax1657 (b), in pure and mixed gas conditions (pink curve for pure gas, green curve using the binary mixture CO_2/N_2 (15:85 v/v), gray curve using the binary CO_2/CH_4 (35:65 v/v).

CONCLUSIONS

In summary, we have reported a novel chiral 3D MOF, derived from the natural amino acid *L*-histidine exhibiting a **qtz-e**-type topology for the first time in a MOF. This novel material shows a reversible and continuous breathing, as evidenced by *in situ* SCXRD, which leads to a stable guest-free phase with a drastic reduction of the unit-cell volume and the size of the channels. The process can be reversed by exposing the sample to open-air or gases like Ar, N_2, CO_2 and C_3H_6 which also originates two-step adsorption isotherms for Ar, N_2 and CO_2. The use of *in situ* SCXRD at the Synchrotron Light Source allowed the resolution of the crystal structures of 4 different host-guest adsorbates (Ar, N_2, CO_2 and C_3H_6), offering unprecedented snapshots on the mechanisms governing the gas adsorption of these gases. The MOF **1** is able to efficiently separate mixtures of CO_2/N_2, CO_2/CH_4 and C_3H_8/C_3H_6. These separations have been investigated with the MOF packed in a column and integrated in a mixed matrix membrane (MMM), which provides fundamental insight into the properties of the materials and the guest-host interactions in the pure MOFs and in the MMMs. The results of our study are of great practical importance for the potential use in the separation of economically or environmentally important gas mixtures, such as CO_2/CH_4 separation from natural gas or from biogas, CO_2/N_2 separation from flue gas, or olefin/paraffin separation in the petrochemical industry. Considering the possibility to tailor the pore size and internal chemistry, further application of these materials in a much wider field, for instance catalysis, can also be hypothesized.

EXPERIMENTAL SECTION

Preparation of Cu^{II}_2(S,S)-hismox · $5H_2O$ (1): Well-formed deep blue cubic prisms of **1**, suitable for X-ray diffraction, were grown after a few days of slow layer diffusion in an essay tube at room temperature. The top layer was a pH = 2 aqueous solution (12 mL, pH was adjusted using HCl), while the bottom one was another aqueous solution of $(Bu_4N)_2\{Cu_2[(S,S)\text{-hismox}](OH)_2\} \cdot 4H_2O$ (0.1 mmol dissolved in 2 mL of water). The crystals were collected by filtration and air-dried (0.045 g, 77% yield); elemental analysis calculated (%) for $C_{14}H_{22}Cu_2N_6O_{11}$ (577.5): C 29.12, H 3.84, N 14.55; found: C 29.06, H 3.77, N 14.61. IR (KBr) 3376 cm^{-1} (ν_{N-H}) and 1608 cm^{-1} ($\nu_{C=O}$).

Alternatively, a gram-scale synthesis of **1** can be also carried out: 2.5 g (2.32 mmol) of $(Bu_4N)_2\{Cu_2[(S,S)\text{-hismox}](OH)_2\} \cdot 4H_2O$ were dissolved in 25 mL of H_2O. To the resulting dark green solution, another aqueous acid solution (HCl, pH = 2) was added slowly, under a continuous stirring, to reach a final pH value of *ca.* 4.0. The blue polycrystalline solid that appeared was filtered off, washed with water and methanol and dried under vacuum. Yield: 1.21 g, 91%; Anal.: calcd for $C_{14}H_{22}Cu_2N_6O_{11}$ (577.5): C 29.12, H 3.84, N 14.55; found: C 29.11, H 3.70, N 14.59. IR (KBr) 3356 cm^{-1} (ν_{N-H}) and 1612 cm^{-1} ($\nu_{C=O}$).

Membrane preparation. All pure Pebax®1657 and MMMs were cast from water and ethanol (ratio 30:70 wt%/wt%) mixture -based solutions or suspensions that were poured into level Teflon dishes. Slow solvent-evaporation yielded self-standing films that were blue in color for all MMMs, as exemplified in Figure 9a. The Pebax1657/MOFs weight ratios were 10:1, 10:2, 10:3 and 10:4, corresponding to MOFs volume percentages of 6 vol%, 12 vol%, 17 vol% and 22 vol%, respectively.

ASSOCIATED CONTENT

Supporting Information Available. Physical techniques. Crystallographic and catalytic details. Figures S1–S31. Tables S1–S2. CCDC reference numbers 1891576-1891596. Methods for morphological and gas transport determination of MMMs. This material is available free of charge via the Internet at http://pubs.acs.org.

AUTHOR INFORMATION

Corresponding Author

* To whom correspondence should be addressed. E–mail: jesus.ferrando@uv.es; donatella.armentano@unical.it; emilio.pardo@uv.es.

Notes

The authors declare no competing financial interests.

ACKNOWLEDGMENT

This work was supported by the MINECO (Spain) (Projects CTQ2016-75671-P, MAT2017-86992-R, MAT-80285-P and Excellence Unit "Maria de Maeztu" MDM-2015-0538) and the Ministero dell'Istruzione, dell'Università e della Ricerca (Italy). M. M. and E. T. thank the MINECO and R.B. thanks the MIUR (Project PON R&I FSE-FESR 2014-2020) for predoctoral grants. Thanks are also extended to the Ramón y Cajal Program (E. P.), the "Fondo per il finanziamento delle attività base di ricerca" (D.A.), and the "Suprograma atracció de talent-contractes postdoctorals de la Universitat de Valencia" (J. F.-S.). E.P. acknowledges the financial support of the European Research Council under the European Union's Horizon 2020 research and innovation programme / ERC Grant Agreement No 814804, MOF-reactors. We acknowledge Diamond Light Source for awarded beamtime and provision of synchrotron radiation facilities with dosing gas cell and thank Dr Mark Warren for his assistance at I19 beamline(Proposal number MT18768-2). Finally, we also acknowledge Alba synchrotron for the beamtime (Proposal ID 2018022631) and thank Dr. Aleksandr Missiul for his assistance at MSPD-BL04.

REFERENCES

(1) Furukawa, H.; Cordova, K. E.; O'Keeffe, M.; Yaghi, O. M. The Chemistry and Applications of Metal-Organic Frameworks. *Science* **2013**, *341*, 974. https://doi.org/10.1126/science.1230444.

(2) Long, J. R.; Yaghi, O. M. The Pervasive Chemistry of Metal-Organic Frameworks. *Chem. Soc. Rev.* **2009**, *38* (5), 1213–1214. https://doi.org/10.1039/b903811f.

(3) Zhou, H.-C.; Kitagawa, S. Metal–Organic Frameworks (MOFs). *Chem. Soc. Rev.* **2014**, *43* (16), 5415–5418. https://doi.org/10.1039/C4CS90059F.

(4) Kitagawa, S.; Matsuda, R. Chemistry of Coordination Space of Porous Coordination Polymers. *Coord. Chem. Rev.* **2007**, *251* (21–24), 2490–2509. https://doi.org/10.1016/j.ccr.2007.07.009.

(5) Li, B.; Wen, H.-M.; Zhou, W.; Xu, J. Q.; Chen, B. Porous Metal-Organic Frameworks: Promising Materials for Methane Storage. *Chem* **2016**, *1* (4), 557–580. https://doi.org/10.1016/j.chempr.2016.09.009.

(6) Lin, R.-B.; Xiang, S.; Xing, H.; Zhou, W.; Chen, B. Exploration of Porous Metal–Organic Frameworks for Gas

Separation and Purification. *Coord. Chem. Rev.* **2019**, *378*, 87–103. https://doi.org/10.1016/j.ccr.2017.09.027.

(7) Mon, M.; Rivero-Crespo, M. A.; Ferrando-Soria, J.; Vidal-Moya, A.; Boronat, M.; Leyva-Pérez, A.; Corma, A.; Hernández-Garrido, J. C.; López-Haro, M.; Calvino, J. J.; et al. Synthesis of Densely Packaged, Ultrasmall Pt 0 2 Clusters within a Thioether-Functionalized MOF: Catalytic Activity in Industrial Reactions at Low Temperature. *Angew. Chemie Int. Ed.* **2018**, *57* (21), 6186–6191. https://doi.org/10.1002/anie.201801957.

(8) Rivero-Crespo, M. A.; Mon, M.; Ferrando-Soria, J.; Lopes, C. W.; Boronat, M.; Leyva-Pérez, A.; Corma, A.; Hernández-Garrido, J. C.; López-Haro, M.; Calvino, J. J.; et al. Confined Pt11+-Water Clusters in a MOF Catalyze the Low-Temperature Water-Gas Shift Reaction with Both CO2 Oxygen Atoms Coming from Water. *Angew. Chemie Int. Ed.* **2018**. *57* (52), 17094–17099. https://doi.org/10.1002/anie.201810251.

(9) Fortea-Pérez, F. R.; Mon, M.; Ferrando-Soria, J.; Boronat, M.; Leyva-Pérez, A.; Corma, A.; Herrera, J. M.; Osadchii, D.; Gascon, J.; Armentano, D.; et al. The MOF-Driven Synthesis of Supported Palladium Clusters with Catalytic Activity for Carbene-Mediated Chemistry. *Nat. Mater.* **2017**, *16* (7), 760–766. https://doi.org/10.1038/nmat4910.

(10) Tejeda-Serrano, M.; Mon, M.; Ross, B.; Gonell, F.; Ferrando-Soria, J.; Corma, A.; Leyva-Pérez, A.; Armentano, D.; Pardo, E. Isolated Fe(III)–O Sites Catalyze the Hydrogenation of Acetylene in Ethylene Flows under Front-End Industrial Conditions. *J. Am. Chem. Soc.* **2018**, *140* (28), 8827–8832. https://doi.org/10.1021/jacs.8b04669.

(11) Ferrando-Soria, J.; Vallejo, J.; Castellano, M.; Martínez-Lillo, J.; Pardo, E.; Cano, J.; Castro, I.; Lloret, F.; Ruiz-García, R.; Julve, M. Molecular Magnetism, Quo Vadis? A Historical Perspective from a Coordination Chemist Viewpoint☆. *Coord. Chem. Rev.* **2017**, *339*, 17–103. https://doi.org/10.1016/j.ccr.2017.03.004.

(12) Darago, L. E.; Aubrey, M. L.; Yu, C. J.; Gonzalez, M. I.; Long, J. R. Electronic Conductivity, Ferrimagnetic Ordering, and Reductive Insertion Mediated by Organic Mixed-Valence in a Ferric Semiquinoid Metal–Organic Framework. *J. Am. Chem. Soc.* **2015**, *137* (50), 15703–15711. https://doi.org/10.1021/jacs.5b10385.

(13) Kim, H.; Yang, S.; Rao, S. R.; Narayanan, S.; Kapustin, E. A.; Furukawa, H.; Umans, A. S.; Yaghi, O. M.; Wang, E. N. Water Harvesting from Air with Metal-Organic Frameworks Powered by Natural Sunlight. *Science* **2017**, *356* (6336), 430–434. https://doi.org/10.1126/science.aam8743.

(14) Cohen, S. M. The Postsynthetic Renaissance in Porous Solids. *J. Am. Chem. Soc.* **2017**, *139* (8), 2855–2863. https://doi.org/10.1021/jacs.6b11259.

(15) Mon, M.; Ferrando-Soria, J.; Verdaguer, M.; Train, C.; Paillard, C.; Dkhil, B.; Versace, C.; Bruno, R.; Armentano, D.; Pardo, E. Postsynthetic Approach for the Rational Design of Chiral Ferroelectric Metal–Organic Frameworks. *J. Am. Chem. Soc.* **2017**, *139* (24), 8098–8101. https://doi.org/10.1021/jacs.7b03633.

(16) Grancha, T.; Ferrando-Soria, J.; Zhou, H.-C.; Gascon, J.; Seoane, B.; Pasán, J.; Fabelo, O.; Julve, M.; Pardo, E. Postsynthetic Improvement of the Physical Properties in a Metal-Organic Framework through a Single Crystal to Single Crystal Transmetallation. *Angew. Chemie Int. Ed.* **2015**, *54* (22), 6521–6525. https://doi.org/10.1002/anie.201501691.

(17) Bradshaw, D.; Claridge, J. B.; Cussen, E. J.; Prior, T. J.; Rosseinsky, M. J. Design, Chirality, and Flexibility in Nanoporous Molecule-Based Materials. *Acc. Chem. Res.* **2005**, *38* (4), 273–282. https://doi.org/10.1021/ar0401606.

(18) Rabone, J.; Yue, Y.-F.; Chong, S. Y.; Stylianou, K. C.; Bacsa, J.; Bradshaw, D.; Darling, G. R.; Berry, N. G.; Khimyak, Y. Z.; Ganin, A. Y.; et al. An Adaptable Peptide-Based Porous Material. *Science* **2010**, *329* (5995), 1053–1057. https://doi.org/10.1126/science.1190672.

(19) Warren, J. E.; Perkins, C. G.; Jelfs, K. E.; Boldrin, P.; Chater, P. A.; Miller, G. J.; Manning, T. D.; Briggs, M. E.; Stylianou, K. C.; Claridge, J. B.; et al. Shape Selectivity by Guest-Driven Restructuring of a Porous Material. *Angew. Chemie Int. Ed.* **2014**, *53* (18), 4592–4596. https://doi.org/10.1002/anie.201307656.

(20) Bloch, W. M.; Champness, N. R.; Doonan, C. J. X-Ray Crystallography in Open-Framework Materials. *Angew. Chemie Int. Ed.* **2015**, *54* (44), 12860–12867. https://doi.org/10.1002/anie.201501545.

(21) Gándara, F.; Bennett, T. D. Crystallography of Metal–Organic Frameworks. *IUCrJ* **2014**, *1* (6), 563–570. https://doi.org/10.1107/S2052252514020351.

(22) Rissanen, K. Crystallography of Encapsulated Molecules. *Chem. Soc. Rev.* **2017**, *46* (9), 2638–2648. https://doi.org/10.1039/C7CS00090A.

(23) Wriedt, M.; Sculley, J. P.; Yakovenko, A. A.; Ma, Y.; Halder, G. J.; Balbuena, P. B.; Zhou, H.-C. Low-Energy Selective Capture of Carbon Dioxide by a Pre-Designed Elastic Single-Molecule Trap. *Angew. Chemie Int. Ed.* **2012**, *51* (39), 9804–9808. https://doi.org/10.1002/anie.201202992.

(24) Yang, S.; Sun, J.; Ramirez-Cuesta, A. J.; Callear, S. K.; David, W. I. F.; Anderson, D. P.; Newby, R.; Blake, A. J.; Parker, J. E.; Tang, C. C.; et al. Selectivity and Direct Visualization of Carbon Dioxide and Sulfur Dioxide in a Decorated Porous Host. *Nat. Chem.* **2012**, *4* (11), 887–894. https://doi.org/10.1038/nchem.1457.

(25) McDonald, T. M.; Mason, J. A.; Kong, X.; Bloch, E. D.; Gygi, D.; Dani, A.; Crocellà, V.; Giordanino, F.; Odoh, S. O.; Drisdell, W. S.; et al. Cooperative Insertion of CO2 in Diamine-Appended Metal-Organic Frameworks. *Nature* **2015**, *519* (7543), 303–308. https://doi.org/10.1038/nature14327.

(26) Giménez-Marqués, M.; Calvo Galve, N.; Palomino, M.; Valencia, S.; Rey, F.; Sastre, G.; Vitórica-Yrezábal, I. J.; Jiménez-Ruiz, M.; Rodríguez-Velamazán, J. A.; González, M. A.; et al. Gas Confinement in Compartmentalized Coordination Polymers for Highly Selective Sorption. *Chem. Sci.* **2017**, *8* (4), 3109–3120. https://doi.org/10.1039/C6SC05122G.

(27) Bloch, E. D.; Murray, L. J.; Queen, W. L.; Chavan, S.; Maximoff, S. N.; Bigi, J. P.; Krishna, R.; Peterson, V. K.; Grandjean, F.; Long, G. J.; et al. Selective Binding of O 2 over N 2 in a Redox–Active Metal–Organic Framework with Open Iron(II) Coordination Sites. *J. Am. Chem. Soc.* **2011**, *133* (37), 14814–14822. https://doi.org/10.1021/ja205976v.

(28) Bloch, E. D.; Queen, W. L.; Krishna, R.; Zadrozny, J. M.; Brown, C. M.; Long, J. R. Hydrocarbon Separations in a Metal-Organic Framework with Open Iron(II) Coordination Sites. *Science* **2012**, *335* (6076), 1606–1610. https://doi.org/10.1126/science.1217544.

(29) Xiang, S.; He, Y.; Zhang, Z.; Wu, H.; Zhou, W.; Krishna, R.; Chen, B. Microporous Metal-Organic Framework with Potential for Carbon Dioxide Capture at Ambient Conditions. *Nat. Commun.* **2012**, *3* (1), 954. https://doi.org/10.1038/ncomms1956.

(30) Geier, S. J.; Mason, J. A.; Bloch, E. D.; Queen, W. L.; Hudson, M. R.; Brown, C. M.; Long, J. R. Selective Adsorption of Ethylene over Ethane and Propylene over Propane in the Metal–Organic Frameworks M2(Dobdc) (M = Mg, Mn, Fe, Co, Ni, Zn). *Chem. Sci.* **2013**, *4* (5), 2054. https://doi.org/10.1039/c3sc00032j.

(31) Bloch, E. D.; Hudson, M. R.; Mason, J. a.; Chavan, S.; Crocellà, V.; Howe, J. D.; Lee, K.; Dzubak, A. L.; Queen, W. L.; Zadrozny, J. M.; et al. Reversible CO Binding Enables Tunable CO/H_2 and CO/N_2 Separations in Metal–Organic Frameworks with Exposed Divalent Metal Cations. *J. Am. Chem. Soc.* **2014**, *136* (30), 10752–10761. https://doi.org/10.1021/ja505318p.

(32) Lee, K.; Isley, W. C.; Dzubak, A. L.; Verma, P.; Stoneburner, S. J.; Lin, L.-C.; Howe, J. D.; Bloch, E. D.; Reed, D. A.; Hudson, M. R.; et al. Design of a Metal–Organic Framework with Enhanced Back Bonding for Separation of N 2 and CH 4. *J. Am. Chem. Soc.* **2014**, *136* (2), 698–704. https://doi.org/10.1021/ja4102979.

(33) Lee, J. S.; Vlaisavljevich, B.; Britt, D. K.; Brown, C. M.; Haranczyk, M.; Neaton, J. B.; Smit, B.; Long, J. R.; Queen, W. L. Understanding Small-Molecule Interactions in Metal-Organic Frameworks: Coupling Experiment with Theory. *Adv. Mater.* **2015**, *27* (38), 5785–5796. https://doi.org/10.1002/adma.201500966.

(34) Li, L.; Lin, R.-B.; Krishna, R.; Wang, X.; Li, B.; Wu, H.; Li, J.; Zhou, W.; Chen, B. Flexible–Robust Metal–Organic Framework for Efficient Removal of Propyne from Propylene. *J. Am. Chem. Soc.* **2017**, *139* (23), 7733–7736. https://doi.org/10.1021/jacs.7b04268.

(35) Hobday, C. L.; Woodall, C. H.; Lennox, M. J.; Frost, M.; Kamenev, K.; Düren, T.; Morrison, C. A.; Moggach, S. A. Understanding the Adsorption Process in ZIF-8 Using High Pressure Crystallography and Computational Modelling. *Nat. Commun.* **2018**, *9* (1), 1429. https://doi.org/10.1038/s41467-018-03878-6.

(36) Miller, S. R.; Wright, P. A.; Devic, T.; Serre, C.; Férey, G.; Llewellyn, P. L.; Denoyel, R.; Gaberova, L.; Filinchuk, Y. Single Crystal X-Ray Diffraction Studies of Carbon Dioxide and Fuel-Related Gases Adsorbed on the Small Pore Scandium Terephthalate Metal Organic Framework, Sc 2 (O 2 CC 6 H 4 CO 2) 3. *Langmuir* **2009**, *25* (6), 3618–3626. https://doi.org/10.1021/la803788u.

(37) Rowsell, J. L. C.; Spencer, E. C.; Eckert, J.; Howard, J. A. K.; Yaghi, O. M. Gas Adsorption Sites in a Large-Pore Metal-Organic Framework. *Science* **2005**, *309* (5739), 1350–1354. https://doi.org/10.1126/science.1113247.

(38) Xie, L.-H.; Lin, J.-B.; Liu, X.-M.; Wang, Y.; Zhang, W.-X.; Zhang, J.-P.; Chen, X.-M. Porous Coordination Polymer with Flexibility Imparted by Coordinatively Changeable Lithium Ions on the Pore Surface. *Inorg. Chem.* **2010**, *49* (3), 1158–1165. https://doi.org/10.1021/ic902077j.

(39) Zhang, J.-P.; Chen, X.-M. Exceptional Framework Flexibility and Sorption Behavior of a Multifunctional Porous Cuprous Triazolate Framework. *J. Am. Chem. Soc.* **2008**, *130* (18), 6010–6017. https://doi.org/10.1021/ja800550a.

(40) Gonzalez, M. I.; Mason, J. A.; Bloch, E. D.; Teat, S. J.; Gagnon, K. J.; Morrison, G. Y.; Queen, W. L.; Long, J. R. Structural Characterization of Framework–Gas Interactions in the Metal–Organic Framework Co 2 (Dobdc) by in Situ Single-Crystal X-Ray Diffraction. *Chem. Sci.* **2017**, *8* (6), 4387–4398. https://doi.org/10.1039/C7SC00449D.

(41) Carrington, E. J.; Vitórica-Yrezábal, I. J.; Brammer, L. Crystallographic Studies of Gas Sorption in Metal–Organic Frameworks. *Acta Crystallogr. Sect. B Struct. Sci. Cryst. Eng. Mater.* **2014**, *70* (3), 404–422. https://doi.org/10.1107/S2052520614009834.

(42) Lee, J. H.; Jeoung, S.; Chung, Y. G.; Moon, H. R. Elucidation of Flexible Metal-Organic Frameworks: Research Progresses and Recent Developments. *Coord. Chem. Rev.* **2019**, *389*, 161–188. https://doi.org/10.1016/j.ccr.2019.03.008.

(43) Luo, F.; Yan, C.; Dang, L.; Krishna, R.; Zhou, W.; Wu, H.; Dong, X.; Han, Y.; Hu, T.-L.; O'Keeffe, M.; et al. UTSA-74: A MOF-74 Isomer with Two Accessible Binding Sites per Metal Center for Highly Selective Gas Separation. *J. Am. Chem. Soc.* **2016**, *138* (17), 5678–5684. https://doi.org/10.1021/jacs.6b02030.

(44) Brunet, G.; Safin, D. A.; Aghaji, M. Z.; Robeyns, K.; Korobkov, I.; Woo, T. K.; Murugesu, M. Stepwise Crystallographic Visualization of Dynamic Guest Binding in a Nanoporous Framework. *Chem. Sci.* **2017**, *8* (4), 3171–3177. https://doi.org/10.1039/C7SC00267J.

(45) Liao, P.-Q.; Zhou, D.-D.; Zhu, A.-X.; Jiang, L.; Lin, R.-B.; Zhang, J.-P.; Chen, X.-M. Strong and Dynamic CO 2 Sorption in a Flexible Porous Framework Possessing Guest Chelating Claws. *J. Am. Chem. Soc.* **2012**, *134* (42), 17380–17383. https://doi.org/10.1021/ja3073512.

(46) Zhang, J.-P.; Zhu, A.-X.; Chen, X.-M. Single-Crystal X-Ray Diffraction and Raman Spectroscopy Studies of Isobaric N2 Adsorption in SOD-Type Metal–Organic Zeolites. *Chem. Commun.* **2012**, *48* (93), 11395. https://doi.org/10.1039/c2cc35544b.

(47) Lin, J.-B.; Xue, W.; Zhang, J.-P.; Chen, X.-M. An Ionic Porous Coordination Framework Exhibiting High CO 2 Affinity and CO 2 /CH 4 Selectivity. *Chem. Commun.* **2011**, *47* (3), 926–928. https://doi.org/10.1039/C0CC04089D.

(48) Maji, T. K.; Mostafa, G.; Matsuda, R.; Kitagawa, S. Guest-Induced Asymmetry in a Metal−Organic Porous Solid with Reversible Single-Crystal-to-Single-Crystal Structural Transformation. *J. Am. Chem. Soc.* **2005**, *127* (49), 17152–17153. https://doi.org/10.1021/ja0561439.

(49) Kim, H.; Samsonenko, D. G.; Das, S.; Kim, G.-H.; Lee, H.-S.; Dybtsev, D. N.; Berdonosova, E. A.; Kim, K. Methane Sorption and Structural Characterization of the Sorption Sites in Zn 2 (Bdc) 2 (Dabco) by Single Crystal X-Ray Crystallography. *Chem. Asian J.* **2009**, *4* (6), 886–891. https://doi.org/10.1002/asia.200900020.

(50) Vaidhyanathan, R.; Iremonger, S. S.; Shimizu, G. K. H.; Boyd, P. G.; Alavi, S.; Woo, T. K. Direct Observation and Quantification of CO 2 Binding Within an Amine-Functionalized Nanoporous Solid. *Science* **2010**, *330* (6004), 650–653. https://doi.org/10.1126/science.1194237.

(51) Férey, G.; Serre, C. Large Breathing Effects in Three-Dimensional Porous Hybrid Matter: Facts, Analyses, Rules and Consequences. *Chem. Soc. Rev.* **2009**, *38* (5), 1380. https://doi.org/10.1039/b804302g.

(52) Schneemann, A.; Bon, V.; Schwedler, I.; Senkovska, I.; Kaskel, S.; Fischer, R. A. Flexible Metal–Organic Frameworks. *Chem. Soc. Rev.* **2014**, *43* (16), 6062–6096. https://doi.org/10.1039/C4CS00101J.

(53) Carrington, E. J.; McAnally, C. A.; Fletcher, A. J.; Thompson, S. P.; Warren, M.; Brammer, L. Solvent-Switchable Continuous-Breathing Behaviour in a Diamondoid Metal–Organic Framework and Its Influence on CO_2 versus CH_4 Selectivity. *Nat. Chem.* **2017**, *9* (9), 882–889. https://doi.org/10.1038/nchem.2747.

(54) Grancha, T.; Mon, M.; Ferrando-Soria, J.; Gascon, J.; Seoane, B.; Ramos-Fernandez, E. V.; Armentano, D.; Pardo, E. Tuning the Selectivity of Light Hydrocarbons in Natural Gas in a Family of Isoreticular MOFs. *J. Mater. Chem. A* **2017**, *5* (22), 11032–11039. https://doi.org/10.1039/C7TA01179B.

(55) Mon, M.; Qu, X.; Ferrando-Soria, J.; Pellicer-Carreño, I.; Sepúlveda-Escribano, A.; Ramos-Fernandez, E. V.; Jansen, J. C.; Armentano, D.; Pardo, E. Fine-Tuning of the Confined Space in Microporous Metal–Organic Frameworks for Efficient Mercury Removal. *J. Mater. Chem. A* **2017**, *5* (38), 20120–20125. https://doi.org/10.1039/C7TA06199D.

(56) Grancha, T.; Qu, X.; Julve, M.; Ferrando-Soria, J.; Armentano, D.; Pardo, E. Rational Synthesis of Chiral Metal–Organic Frameworks from Preformed Rodlike Secondary Building Units. *Inorg. Chem.* **2017**, *56* (11), 6551–6557. https://doi.org/10.1021/acs.inorgchem.7b00681.

(57) Mon, M.; Ferrando-Soria, J.; Grancha, T.; Fortea-Pérez, F. R.; Gascon, J.; Leyva-Pérez, A.; Armentano, D.; Pardo, E. Selective Gold Recovery and Catalysis in a Highly Flexible Methionine-Decorated Metal–Organic Framework. *J. Am. Chem. Soc.* **2016**, *138* (25), 7864–7867. https://doi.org/10.1021/jacs.6b04635.

(58) Grancha, T.; Mon, M.; Ferrando-Soria, J.; Armentano, D.; Pardo, E. Structural Studies on a New Family of Chiral BioMOFs. *Cryst. Growth Des.* **2016**, *16* (9), 5571–5578. https://doi.org/10.1021/acs.cgd.6b01052.

(59) Grancha, T.; Ferrando-Soria, J.; Cano, J.; Amorós, P.; Seoane, B.; Gascon, J.; Bazaga-García, M.; Losilla, E. R.; Cabeza, A.; Armentano, D.; et al. Insights into the Dynamics of Grotthuss Mechanism in a Proton-Conducting Chiral Bio MOF. *Chem. Mater.* **2016**, *28* (13), 4608–4615. https://doi.org/10.1021/acs.chemmater.6b01286.

(60) Mon, M.; Lloret, F.; Ferrando-Soria, J.; Martí-Gastaldo, C.; Armentano, D.; Pardo, E. Selective and Efficient Removal of Mercury from Aqueous Media with the Highly Flexible Arms of a BioMOF. *Angew. Chemie Int. Ed.* **2016**, *55* (37), 11167–11172. https://doi.org/10.1002/anie.201606015.

(61) Mellot-Draznieks, C.; Serre, C.; Surblé, S.; Audebrand, N.; Férey, G. Very Large Swelling in Hybrid Frameworks: A Combined Computational and Powder Diffraction Study. *J. Am. Chem. Soc.*

2005, *127* (46), 16273–16278. https://doi.org/10.1021/ja054900x.

(62) Serre, C.; Mellot-Draznieks, C.; Surble, S.; Audebrand, N.; Filinchuk, Y.; Ferey, G. Role of Solvent-Host Interactions That Lead to Very Large Swelling of Hybrid Frameworks. *Science* **2007**, *315* (5820), 1828–1831. https://doi.org/10.1126/science.1137975.

(63) Sholl, D. S.; Lively, R. P. Seven Chemical Separations to Change the World. *Nature* **2016**, *532* (7600), 435–437. https://doi.org/10.1038/532435a.

(64) Oak Ridge National Lab. (ORNL), Oak Ridge, T. (USA). *Materials for Separation Technologies. Energy and Emission Reduction Opportunities*; 2005. https://doi.org/10.2172/1218755.

(65) See https://topospro.com/software/toris/ (accessed Sept 3, 596 2018).

(66) De Lange, M. F.; Vlugt, T. J. H.; Gascon, J.; Kapteijn, F. Adsorptive Characterization of Porous Solids: Error Analysis Guides the Way. *Microporous Mesoporous Mater.* **2014**, *200*, 199–215. https://doi.org/10.1016/j.micromeso.2014.08.048.

(67) Morris, R. E.; Brammer, L. Coordination Change, Lability and Hemilability in Metal–Organic Frameworks. *Chem. Soc. Rev.* **2017**, *46* (17), 5444–5462. https://doi.org/10.1039/C7CS00187H.

(68) McHugh, L. N.; McPherson, M. J.; McCormick, L. J.; Morris, S. A.; Wheatley, P. S.; Teat, S. J.; McKay, D.; Dawson, D. M.; Sansome, C. E. F.; Ashbrook, S. E.; et al. Hydrolytic Stability in Hemilabile Metal–Organic Frameworks. *Nat. Chem.* **2018**, *10* (11), 1096–1102. https://doi.org/10.1038/s41557-018-0104-x.

(69) Krishna, R.; Long, J. R. Screening Metal–Organic Frameworks by Analysis of Transient Breakthrough of Gas Mixtures in a Fixed Bed Adsorber. *J. Phys. Chem. C* **2011**, *115* (26), 12941–12950. https://doi.org/10.1021/jp202203c.

(70) Seoane, B.; Coronas, J.; Gascon, I.; Benavides, M. E.; Karvan, O.; Caro, J.; Kapteijn, F.; Gascon, J. Metal–Organic Framework Based Mixed Matrix Membranes: A Solution for Highly Efficient CO 2 Capture? *Chem. Soc. Rev.* **2015**, *44* (8), 2421–2454. https://doi.org/10.1039/C4CS00437J.

(71) Chuah, C. Y.; Goh, K.; Yang, Y.; Gong, H.; Li, W.; Karahan, H. E.; Guiver, M. D.; Wang, R.; Bae, T. Harnessing Filler Materials for Enhancing Biogas Separation Membranes. *Chem. Rev.* **2018**, *118* (18), 8655–8769. https://doi.org/10.1021/acs.chemrev.8b00091.

(72) Fraga, S. C.; Monteleone, M.; Lanč, M.; Esposito, E.; Fuoco, A.; Giorno, L.; Pilnáček, K.; Friess, K.; Carta, M.; McKeown, N. B.; et al. A Novel Time Lag Method for the Analysis of Mixed Gas Diffusion in Polymeric Membranes by On-Line Mass Spectrometry: Method Development and Validation. *J. Memb. Sci.* **2018**, *561*, 39–58. https://doi.org/10.1016/j.memsci.2018.04.029.

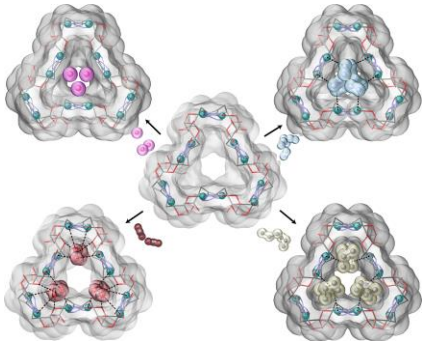

Supporting Information (SI) for the manuscript:

Efficient Gas Separation and Transport Mechanism in Rare Hemilabile Metal-Organic Framework

Marta Mon, Rosaria Bruno, Estefanía Tiburcio, Aida Grau-Atienza, Antonio Sepúlveda-Escribano, Enrique V. Ramos-Fernandez, Alessio Fuoco, Elisa Esposito, Marcello Monteleone, Johannes C. Jansen, Joan Cano, Jesús Ferrando-Soria,* Donatella Armentano* and Emilio Pardo*

Experimental Section

Chemicals

All chemicals were of reagent grade quality. They were purchased from commercial sources and used as received. **H_2Me_2-(*S,S*)-hismox** and **$(Bu_4N)_2\{Cu_2[(S,S)\text{-hismox}](OH)_2\} \cdot 4H_2O$** were prepared as previously reported.[1]

*Preparation of Cu^{II}_2(S,S)-hismox · $5H_2O$ (**1**).*

Well-formed deep blue cubic prisms of **1**, suitable for X-ray diffraction, were grown after a few days of slow layer diffusion in an essay tube at room temperature. The top layer was a pH = 2 aqueous solution (12 mL, pH was adjusted using HCl), while the bottom one was another aqueous solution of $(Bu_4N)_2\{Cu_2[(S,S)\text{-hismox}](OH)_2\} \cdot 4H_2O$ (0.1 mmol dissolved in 2 mL of water). The crystals were collected by filtration and air-dried (0.045 g, 77.% yield); elemental analysis calculated (%) for $C_{14}H_{22}Cu_2N_6O_{11}$ (577.5): C 29.12, H 3.84, N 14.55; found: C 29.06, H 3.77, N 14.61. IR (KBr) 3376 cm^{-1} (ν_{N-H}) and 1608 cm^{-1} ($\nu_{C=O}$).

Alternatively, a gram-scale synthesis of **1** can be also carried out: 2.5 g (2.32 mmol) of $(Bu_4N)_2\{Cu_2[(S,S)\text{-hismox}](OH)_2\} \cdot 4H_2O$ were dissolved in 25 mL of H_2O. To the resulting dark green solution, another aqueous acid solution (HCl, pH = 2) was added slowly, under a continuous stirring, to reach a final pH value of *ca.* 4.0. The blue polycrystalline solid that appeared was filtered off, washed with water and methanol and dried under vacuum. Yield: 1.21 g, 91%; Anal.: calcd for $C_{14}H_{22}Cu_2N_6O_{11}$ (577.5): C 29.12, H 3.84, N 14.55; found: C 29.11, H 3.70, N 14.59. IR (KBr) 3356 cm^{-1} (ν_{N-H}) and 1612 cm^{-1} ($\nu_{C=O}$).

Membrane preparation.

All pure Pebax®1657 and MMMs were cast from water and ethanol (ratio 30:70 wt%/wt%) mixture -based solutions or suspensions that were poured into level Teflon dishes. Slow solvent-evaporation yielded self-standing films that were blue in colour for all MMMs, as exemplified in Figure 9a. The Pebax1657/MOFs weight ratios were 10:1,

10:2, 10:3 and 10:4, corresponding to MOFs volume percentages of 6 vol%, 12 vol%, 17 vol% and 22 vol%, respectively.

Physical Techniques

Elemental (C, H, N), and ICP-MS analyses were performed at the Microanalytical Service of the Universitat de València. FT–IR spectra were recorded on a Perkin-Elmer 882 spectrophotometer as KBr pellets. The thermogravimetric analysis was performed on crystalline samples under a dry N_2 atmosphere with a Mettler Toledo TGA/STDA 851^e thermobalance operating at a heating rate of 10 ºC min^{-1}.

X-ray Powder Diffraction Measurements: A fresh polycrystalline sample of **1** was introduced into a 0.5 mm borosilicate capillary prior to being mounted and aligned on an Empyrean PANalytical powder diffractometer, using Cu Kα radiation (λ = 1.54056 Å). For each sample, five repeated measurements were collected at room temperature (2θ = 2–60°) and merged in a single diffractogram.

Gas adsorption: The CH_4 (298 K), C_3H_8 (298 K), C_3H_6 (298 K), Ar (77 K), N_2 (77 and 298 K) and CO_2 (195, 273 and 298 K) were carried out on a polycrystalline sample of **1** with a Micromeritics ASAP2020 instrument. Sample was first activated with methanol and then evacuated at 348 K during 24 hours under 10^{-6} Torr prior to their analysis.

Synchrotron powder X-ray diffraction: S-XRPD experiments were collected at the high-pressure/microdiffraction end station of the MSPD beamline at synchrotron ALBA in Spain, using a Rayonix SX165CCD 2D detector and a wavelength of 0.4243 Å. The experiments were performed in an ad hoc capillary reaction cell (fused silica capillary, inner diameter 247μm, outer diameter 662μm). The material was placed inside the capillary connected to a manifold that allows dosing gases at different pressures. An Oxford Cryostream 700 was used to control the temperature of the sample. In a standard experiment the sample is activated at 350 K under vacuum. After the activation, the sample is then pressurized with a given pure gas (N_2, Ar, CO_2 etc.). Then, the temperature is decreased step-wise while the XRD pattern is recorded.

Synchrotron single-crystal X-ray diffraction: The various crystal structures of **1** in the 110-350 K range of temperature and ambient pressure were solved with single-crystal

X-ray diffraction at the Synchrotron Light Source, Diamond, UK. Then *in-situ* SC-XRD experiments were carried out for dehydrated compound **1** at variable temperatures and under the presence of different gases (first H_2O to evidence reversibility of water uptake and then N_2, Ar, CO_2 and C_3H_6) at different pressures, using synchrotron radiation, on single crystal sealed in the gas cell, designed and built at Diamond Light Source, in the I19 beamline to perform *in situ* gas-dosing experiments (Figure S1).

CCDC reference number for all crystal structures CCDC 1891576-1891596.

- *Synchrotron crystallographic measurements and data analysis of **1** at different temperatures.*

A crystal of **1** with 0.05 x 0.04 x 0.04 mm as dimensions was selected and mounted on a MITIGEN holder in glue, then the sample pin was inserted in the glass capillary, sealed in the cell and placed on a liquid nitrogen stream cooled at 110 K. Diffraction data for **1** were collected using synchrotron radiation at I19 beamline in DIAMOND (λ = 0.6889 Å). The data were collected at 110 K and then starting heating to 140-170-200-250-300-320-350 K (see Tables S1-S2). They were processed through xia2 software,[2] and all structures solved with the SHELXS structure solution program, using the Patterson method. The model was refined with version 2013/4 of SHELXL against F^2 on all data by full–matrix least squares.[3]

A slightly positive thermal expansion (PTE) over the temperature range of 110-290 K is followed by an abrupt contraction of *a* and *c* axes and a resulting reduction of the volume at 320 and 350 K (see Tables S1-S3). The large breathing motion is associated with the removal of the water molecules together with the rearrangement (hemilability) of carboxylate groups accounting for a large decrease in the unit-cell volume ($\Delta V \approx 325$ Å^3, ~22%, see Table S1 and following section).

In all solved structures all non–hydrogen atoms of the MOF net were refined anisotropically. The use somewhere of some C–C bond lengths restrains during the refinements in **1**, have been reasonable imposed and related to extraordinary flexibility of the frameworks.

The solvent molecules were well-defined and modelled in all solved structures with data measured in the 110-290 K. The hydrogen atoms of the ligand were set in

calculated positions and refined as riding atoms whereas for water molecules, where possible, were found from ΔF map and then refined with restrains on O-H distance and angle and fixed thermal factors.

The resolution of data measured at 320 and 350 K revealed no significant peaks of electron density attributable to waters in the channels in either case, as would be expected from solvent loss (see section below).

The comments for the main alerts A and B are described in the CIF using the validation reply form (vrf).

A summary of the crystallographic data and structure refinement for the hydrated MOF **1** at different temperatures is given in Table S2.

The final geometrical calculations on free voids and the graphical manipulations were carried out with PLATON implemented in WinGX, and CRYSTAL MAKER programs, respectively.

- *Single-crystal structure determination and refinement of **1** during desolvation and resolvation processes.*

Single crystal of **1** were removed from their water solvent by first washing with methanol then applying vacuum/refill cycles for three times (three minutes for each cycle) and heating *in situ* using cryostream device of the I19 beamline in DIAMOND. Synchrotron crystallographic data were collected on a single selected single crystal of 0.054 x 0.050 x 0.050 mm as dimensions under vacuum at 300, 320 and 350 K and only then cooling down to 110 K and measuring at 250-200-150-110 K (see Table S3). They were processed through xia2 software,[2] and all structures solved with the SHELXS structure solution program, using the Patterson method. The model was refined with version 2013/4 of SHELXL against F^2 on all data by full–matrix least squares.[3]

In all solved structures all non–hydrogen atoms of the MOF net were refined anisotropically. The presence of some C–C bond lengths restrains during the refinements in **1**, have been reasonable imposed and related to both extraordinary flexibility of the frameworks and small effects of heating over the crystal morphology.

While the resolution of data measured at 300, 320 and 350 K and then 260-110 K revealed no significant peaks of electron density attributable to waters in the channels in either case, confirming the evacuation occurred, only the crystal structure measured at 300K (defined as a 'transient' structure) unveiled, surprisingly, a very large positive thermal expansion after evacuation followed by the 'robust' crystal structures exhibiting the expected negative thermal expansion at both 320 and 350 K and 250-110 K (Tables S2 and S3). In fact, as reported in the main text, the dehydrated network is stable and did not show appreciable changes in the range of temperatures (Tables S2 and S3).

After that, valve on sample has been opened for one minute to expose crystal to air and allow to adsorb water vapor and then *in situ* synchrotron data were collected at 260 and 150 K (see Table S4). They were processed through xia2 software,[2] and all structures solved. In all solved structures significant peaks of electron density attributable to waters in the channels clearly appeared confirming the fast and reversible water desolvation-rehydration process occurring in **1**.

A summary of the crystallographic data and structure refinement for the dehydrated and after rehydration process on MOF **1** at different temperatures are given in Tables S2, S3 and S4, respectively.

The final geometrical calculations on free voids and the graphical manipulations were carried out with PLATON implemented in WinGX, and CRYSTAL MAKER programs, respectively.

- *in situ synchrotron SC-XRD measurements and data analysis during gas sorption.*

As stated above, the whole crystallographic studies on single-crystal X-ray on **1** were carried out at beamline I19, at Diamond Light Source. The gas loading was precisely controlled and measured on single crystal sealed in the gas cell, designed and built at Diamond Light Source, to perform *in-situ* gas-dosing experiments. Experiments were carried out on the same single crystal of **1** used for studying dehydration-rehydration process. After activation of the crystal data were acquired measuring on **1** at variable temperatures and under the presence of different gases (N_2, Ar, CO_2 and C_3H_6) at different pressures (see below for refinement details). Once measurements on a given

gas have been performed, the gas was exhausted from main rig and sample lines. Then, vacuum was applied on all the lines to remove any residue of previously measured gas and all the rig and gas lines refilled with inert gas. After closing the inert gas lines, once again the rig and sample lines were exhausted to restart with vacuum and new gas. All the four adsorbate structures were measured at two different T values accordingly to their critical points (see Table S5 for details on T and P).

All data were processed through xia2 software,[2] and solved with the SHELXS structure solution program, using the Patterson method. The models were refined with version 2013/4 of SHELXL against F^2 on all data by full–matrix least squares.[3]

All non–hydrogen atoms of the MOF net were refined anisotropically. The hydrogen atoms of the ligand were set in calculated positions and refined as riding atoms.

The comments for the main alerts A and B are described in the CIF using the validation reply form (vrf).

A summary of the crystallographic data and structure refinement for the (N_2, Ar, CO_2 and C_3H_6) adsorbates of MOF **1** at different temperatures is given in Table S5.

The final geometrical calculations on free voids and the graphical manipulations were carried out with PLATON implemented in WinGX, and CRYSTAL MAKER programs, respectively.

In depth analysis of gas loaded crystal structures:

Overall, analysis of the structures of {Cu_2[(*S*,*S*)-hismox]} · $6N_2$, {Cu_2[(*S*,*S*)-hismox]} · $3CO_2$ and {Cu_2[(*S*,*S*)-hismox]} · $2C_3H_6$ shows that N_2, CO_2 and C_3H_6 interact, axially, with the open coordination site offered by copper(II) ions (Figure 5), confirming that this site has the greatest contribution to the adsorption of these gases in the material (*vide infra*). N_2, Ar, CO_2 and C_3H_6 were also measured at high pressures (10, 9.4 and 7.5 bar, respectively) at different T values accordingly to their critical points (see Table S5 for details on T and P). In these conditions N_2 (only at 110K), CO_2 and Ar guest molecules were unambiguously unveiled (see Single Crystal X-ray Diffraction section at Supporting Information for an in depth analysis of **N_2@1**, **CO_2@1**and **Ar@1** crystal

structures), whereas crystal structures for the C_3H_6 adsorbate have been obtained both at 1 and 7.5 bar (Figures 7 and S15-S21).

{Cu$_2$[(*S*,*S*)-hismox]} · 6N$_2$: The crystal structure has been measured on the evacuated crystal of **1** under a pressure of 7. 4 bar of N_2 at 110 K. Data were acquired also from crystals of **1** loaded with N_2 between temperature and pressures ranges of 298–110 K and 0.5–7.4 bar. Refinement of data collected at 298 K and low pressures (0.5–6 bar) revealed no significant peaks of electron density attributable to guests in the channels in either case, as would be expected from their weak interaction due to thermal motion and low loading. As the temperature was lowered, many local maxima were located in the observed structure factor Fourier maps, providing evidence of the localization of the gas atoms. This localization is most apparent at 110 K.

Well-located N_2 guest molecules were refined with fixed thermal factors due to expected high thermal motion. Both the high thermal factors on guest molecules and high-pressure regime (affecting a bit crystal quality) are most likely at the origin of the moderate high R factor.

The crystal structure of {Cu$_2$[(*S*,*S*)-hismox]} · 6N$_2$ (7.4 bar of N_2 at 110 K, Figure 5a) shows that N_2 molecules adopts three different adsorption sites. The primary adsorption site displays an end-on coordination geometry towards the d^9 Cu(II) metal ion with a Cu–N_{N2} distance of 2.44(6) Å, significantly shorter than Cu–N_{N2} separation of 4.11 Å observed in the unique structure reported so far for porous copper frameworks solved by single crystal X-ray experiment.[4] The non-linear Cu–N–N angle of 122(5)° suggests a significant contribution of back-bonding interaction between N_2 and Cu(II). These two main structural parameters indicate the strongest Cu-N_2 binding reported so far in a MOF. N_2 molecules at 110 K residing in the other two absorption sites, farther from Cu^{2+}, are thermally disordered. The secondary sites (Figures 5a, S15 and S16) display van der Waals interactions between N_2 and the *waving* oxygen atoms of carboxylate groups belonging to hismox ligand, with $N_{N2}\cdots O$ shortest interactions of 2.71(6) and 2.89(6) Å (Figure S15). Besides the net displays the expected expansion followed by a O-CO motion moving the weaker bond at Cu…O to 2.94(1) Å. The additional third adsorption site identified from local maxima of electron density, is situated at the center of the pores (with molecules in special positions) exhibiting as closest contacts with the framework the H_2C- of the histidine moiety [shortest $N_2\cdots$ H-C- at 3.64(6) Å] (Figures

5a and S15e). Full occupancy factors of three adsorption sites give six N_2 molecules adsorbed per formula unit, and corresponds remarkably well to the estimated number of N_2 molecules adsorbed in the framework from the gas adsorption measurement.

{Cu$_2$[(*S*,*S*)-hismox]} · 3CO$_2$: The crystal structures were obtained from a single crystal dosed with 9.4 bar of CO_2 in a sealed capillary at 235 and 298 K. The best model has been reached at 235 K, even if even at 298 K no important variations on the structure has been registered (see Table S5).

Peaks related to CO_2 guest molecules were detected with a fully occupancy factors and refined with restrains on bond lengths and fixed thermal factors due to expected high thermal motion, especially associated with guest molecules occupying the third adsorption sites. At 235 K, CO_2 is found to interact with a large Cu–O_{CO2} distances of 3.033(5) and 3.451(5) Å. This site, found in all refinements over the temperature range examined, can be identified as the primary adsorption site (Figures 5c bottom, S18 and S19). Moreover, O atoms from the carbonyl groups of the ligands are situated at only 2.848(5) Å from the C atom of CO_2 molecules occupying the primary site, suggesting an interaction between the C(δ^+) atom of the CO_2 molecule and the O lone pair, as observed before.[5] The secondary adsorption sites identified, are situated at the center of the pores, where CO_2 molecules are packed with closest contacts with the framework through the H_2C- of the ligand [shortest O-C-O⋯ H-C- at 3.436(6) Å] (Figures 5c and S18b).

{Cu$_2$[(*S*,*S*)-hismox]} · 0.66Ar: SCXRD data from crystals of **1** loaded with Ar were collected firstly between temperature range of 320–100 K at a pressure of 2 bar. Unfortunately, refinement of data revealed no discernible peaks of electron density assignable to guests. Their location became apparent at 120 K under a pressure of 10 bar, even if the population is lower than the loaded amount observed in the gas adsorption measurements. Only one site has been found with shortest contacts with the net at 3.087(9) Å far from H-C- of the histidine moieties (Figure S17). The shortest distance of 3.98 Å with copper metal ions is significantly longer than that recently reported for Co–Ar of 2.932(9) Å reported,[6] which provides a possible explanation for the difficulties finding all adsorbed Ar atoms. This point must be responsible for the lower Ar loading found in the structure –compared to N_2, CO_2 and C_3H_6 adsorbates and gas-sorption measurements– due to the possible higher disorder of these *free* atoms,

which does not allow to define all of them. Furthermore, the resolution of the structure unveiled a network not really 'opened' (see cell volume in Table S5) most likely as consequence of no change in copper coordination environment.

{Cu_2[(*S*,*S*)-hismox]} · 2C_3H_6: These crystal structures have obtained both at pressures of 1 and 7.5 bar, and temperature of 230 and 290 K, respectively.

Refinements of both data collected at high and low pressure (290 K / 7.5 bar and 230 K / 1 bar) revealed significant electron density attributable to C_3H_6 guests in the channels. The local maxima were located in both the observed structure factor Fourier maps, providing the first single-crystal structures determination of a metal–C_3H_6 interaction. Guest molecules were detected with a fully occupancy factors in all structures and refined with restrains on bond lengths. Hydrogen on guests have been neither found nor calculated. As a consequence of a large thermal motion they exhibit high thermal factors. These high thermal factors on guest molecules and also the high-pressure regime used (affecting a bit crystal quality) are most likely at the origin of the moderate high R factor (Table S5).

Breakthrough measurements: Breakthrough curve experiments for three different mixtures of gases CH_4/CO_2 (75/25), N_2/CO_2 (75/25) and C_3H_8/C_3H_6 (50/50) were carried out using a column at 298 K. The sample powder was packed in the middle part of the column. Here, the sample mass we used is *ca.* 1 g. Breakthrough allows *in situ* activation of the sample under Helium flow. Mass flow controllers controlled the flow rates of all gases. Before the measurement, the sample was activated at the desired temperature for 19 hours. The gas stream from the outlet of the column was analysed online with a mass spectrometer. The preparation of a fixed bed for breakthrough experiments is not a trivial point. When activated carbons or zeolites are used for breakthrough, the powders are pelletized, in order to get and controlled particle size and furthermore the bed is compressed. In this way it is possible to achieve a quasi-plug flow or piston flow through the column. In the case of MOFs, the difficulties to prepare pellets or the stability issues that many MOFs present upon compression, limit the degree of freedom to prepare fixed beds that allows a quasi-piston flow through the bed. For that reason, we used inert gas (H_2) that allows us to track the deviation of the flow from the ideal flow. The amount of gas adsorbed was the difference between the shape

of the CH_4, N_2, CO_2, C_3H_8 and C_3H_6 breakthrough and the H_2 breakthrough. Thus, the dispersion and the very small pressure drop can be considered.

Membranes characterization:

- *Structural and morphological characterization.*

Morphological analysis of membranes were performed by scanning electron microscopy (SEM) on a Phenom Pro X desktop SEM, equipped with backscattering detector (Phenom-World B.V., Netherlands).

- *Determination of gas transport properties.*

Single gas permeation tests were carried out at 25 °C and at a feed pressure of 1 bar, using a fixed-volume pressure increase instrument (ESSR), described elsewhere.[7] Permeability coefficients, P, and diffusion coefficients, D, were determined by the time-lag method.[8] The simplest model of permeation through dense polymeric films describes permeability as the product of diffusion coefficient and solubility coefficient. Thus, the apparent solubility, S, was indirectly calculated as S = P/D. The ideal selectivity is the ratio of permeability of two species, α(A/B) = PA/PB. Mixed gas permeation tests were carried out using a custom made constant pressure/variable volume instrument, described elsewhere,[9,10] equipped with a quadrupole mass filter (HPR-20 QIC Benchtop residual gas analysis system, Hiden Analytical). Measurements were carried out as a sequence of increasing and subsequently decreasing pressure steps in the range from 1-6 bar(a). For the constant pressure/variable volume system, the theoretical permeate flow rate as a function of time curve is given by the equation, describing Fickian diffusion in nonporous film:

$$\varphi_p = \left(\frac{dV}{dt}\right)_0 + Alp_f S\left(\frac{D}{l^2} - \frac{2}{\pi^2}\sum_1^n \frac{(-1)^n}{n^2}\left(-\frac{Dn^2\pi^2}{l^2}\right) exp\left(-\frac{Dn^2\pi^2}{l^2}\right)\right) \qquad \text{(eq. S1)}$$

in which $\boldsymbol{\varphi_P}$ is the permeate flow rate ($cm^3_{STP}\ min^{-1}$) at time, t (s), R is the universal gas constant ($8.314 \times 10^{-5}\ m^3\ bar\ mol^{-1}{\cdot}K^{-1}$), T is the absolute temperature (K), A is the

exposed membrane area (m^2), l is the membrane thickness, p_f is the feed pressure (bar), S is the gas solubility (m^3_{STP} m^{-3} bar^{-1}), and D is the diffusion coefficient (m^2 s^{-1}).

Table S1. Summary of Crystallographic Data for 1@110K, 1@140K 1@170K, 1@200K and 1@250K.

Compound	**1@110K**	**1@140K**	**1@170K**	**1@200K**	**1@250K**
Formula	$C_{14}H_{24}Cu_2N_6O_{12}$	$C_{14}H_{22}Cu_2N_6O_{12}$	$C_{14}H_{22}Cu_2N_6O_{12}$	$C_{14}H_{22}Cu_2N_6O_{12}$	$C_{14}H_{22}Cu_2N_6O_{12}$
M (g mol^{-1})	595.47	595.47	595.47	595.47	595.47
λ (Å)	0.6889	0.6889	0.6889	0.6889	0.6889
Crystal system	trigonal	trigonal	trigonal	trigonal	trigonal
Space group	$P3_121$	$P3_121$	$P3_121$	$P3_121$	$P3_121$
a (Å)	10.5755(2)	10.5867(2)	10.5958(2)	10.6489(3)	10.70450(10)
c (Å)	16.8276(4)	16.8414(4)	16.8456(4)	16.8523(5)	16.8919(3)
V (Å^3)	1629.88(7)	1634.67(8)	1637.89(9)	1655.00(11)	1676.26(4)
Z	3	3	3	3	3
ρ_{calc} (g cm^{-3})	1.820	1.815	1.811	1.792	1.770
μ (mm^{-1})	1.874	1.868	1.864	1.845	1.747
T (K)	110	140	170	200	250
θ range for data collection (°)	2.155- 30.814	2.153- 30.799	2.151- 30.770	2.140 - 30.684	2.129- 30.860
Completeness to θ = 25.0	100%	100%	100%	100%	100%
Measured reflections	19916	20123	20219	19242	21065
Unique reflections	3616	3631	3641	3656	3751
Observed reflections [$I > 2\sigma(I)$]	3316	3154	3072	2985	3603
Goof	1.062	1.044	0.986	1.013	1.028
Absolute structure parameter (Flack)	0.023(5)	0.017(6)	0.012(6)	0.016(8)	0.002(6)
R^a [$I > 2\sigma(I)$] (all data)	0.0329 (0.0357)	0.0329 (0.0378)	0.0324 (0.0384)	0.0362 (0.0462)	0.0355 (0.0367)
wR^b [$I > 2\sigma(I)$] (all data)	0.0990 (0.1005)	0.0989 (0.1006)	0.0952 (0.0973)	0.1053 (0.1085)	0.1172 (0.1195)
CCDC	1891576	1891577	1891578	1891579	1891580

^{a} $\boldsymbol{R = \sum(|F_o| - |F_c|)/\sum|F_o|}$. ^{b} $\boldsymbol{wR = [\sum w(|F_o| - |F_c|)^2/\sum w|F_o|^2]^{1/2}}$.

Table S2. Summary of Crystallographic Data for 1@300K, 1@320K and 1@350K.

Compound	**1@300K**	**1@320K**	**1@350K**
Formula	$C_{14}H_{12}Cu_2N_6O_6$	$C_{14}H_{12}Cu_2N_6O_6$	$C_{14}H_{12}Cu_2N_6O_6$
M (g mol^{-1})	487.38	487.38	487.38
λ (Å)	0.6889	0.6889	0.6889
Crystal system	trigonal	trigonal	trigonal
Space group	$P3_1\,21$	$P3_1\,21$	$P3_1\,21$
a (Å)	10.926(12)	10.0623(16)	10.055(3)
c (Å)	17.70(2)	16.382(3)	16.302(6)
V (Å^3)	1829(4)	1436.4(5)	1427.2(10)
Z	3	3	3
ρ_{calc} (g cm^{-3})	1.327	1.690	1.701
μ (mm^{-1})	1.578	2.010	2.023
T (K)	300	320	350
θ range for data collection (°)	2.086- 30.255	2.265- 30.737	1.521- 28.00
Completeness to θ = 25.0	100%	100%	100%
Measured reflections	19063	16951	17129
Unique reflections	3737	3173	3211
Observed reflections [$I > 2\sigma(I)$]	973	1733	1656
Goof	0.932	0.983	0.977
Absolute structure parameter (Flack)	0.02(5)	0.02(2)	0.01(2)
R^a [$I > 2\sigma(I)$] (all data)	0.0931 (0.2315)	0.0703 (0.1147)	0.0691 (0.1191)
wR^b [$I > 2\sigma(I)$] (all data)	0.2456 (0.2890)	0.1601 (0.1854)	0.1627(0.1903)
CCDC	1891581	1891582	1891583

^{a} $R = \sum(|F_o| - |F_c|)/\sum|F_o|$. ^{b} $wR = [\sum w(|F_o| - |F_c|)^2/\sum w|F_o|^2]^{1/2}$.

Table S3. Summary of Crystallographic Data for dehydrated phase 1@250K, 1@200K, 1@150 and 1@110K.

Compound	**1@250K**	**1@200K**	**1@150K**	**1@110K**
Formula	$C_{14}H_{12}Cu_2N_6O_6$	$C_{14}H_{12}Cu_2N_6O_6$	$C_{14}H_{12}Cu_2N_6O_6$	$C_{14}H_{12}Cu_2N_6O_6$
M (g mol^{-1})	487.38	487.38	487.38	487.38
λ (Å)	0.6889	0.6889	0.6889	0.6889
Crystal system	trigonal	trigonal	trigonal	trigonal
Space group	$P3_1\,21$	$P3_1\,21$	$P3_1\,21$	$P3_1\,21$
a (Å)	10.156(5)	10.125(4)	10.136(2)	10.166(5)
c (Å)	16.664(9)	16.556(9)	16.514(4)	16.563(10)
V (Å^3)	1488.4(16)	1470.0(15)	1469.3(8)	1482.3(17)
Z	3	3	3	3
ρ_{calc} (g cm^{-3})	1.631	1.652	1.652	1.638
μ (mm^{-1})	1.940	1.964	1.965	1.948
T (K)	250	200	150	110
θ range for data collection (°)	2.245 - 24.962	2.548 - 24.997	2.249 - 24.988	2.540 - 24.984
Completeness to θ = 25.0	100%	100%	100%	100 %
Measured reflections	11806	11615	11666	7278
Unique reflections	1918	1900	1901	1885
Observed reflections [$I > 2\sigma(I)$]	1498	1478	1540	1516
Goof	1.076	1.164	1.211	1.187
Absolute structure parameter (Flack)	0.03(3)	0.02(3)	-0.03(2)	-0.04(2)
R^a [$I > 2\sigma(I)$] (all data)	0.0887 (0.1049)	0.0861 (0.1044)	0.0838 (0.0968)	0.0718 (0.0860)
wR^b [$I > 2\sigma(I)$] (all data)	0.2035 (0.2243)	0.2011 (0.2202)	0.1912 (0.2064)	0.1589 (0.1706)
CCDC	1891584	1891585	1891586	1891587

^{a} $\boldsymbol{R = \sum(|F_o| - |F_c|)/\sum|F_o|}$. ^{b} $\boldsymbol{wR = [\sum w(|F_o| - |F_c|)^2/\sum w|F_o|^2]^{1/2}}$.

Table S4. Summary of Crystallographic Data for H_2O@1 at 150K and 260K (Crystal structures after heating the sample to 350 K and single-crystal-exposure to air for one minute, to rehydration).

Compound	**H_2O@1**	**H_2O@1**
Formula	$C_{14}H_{24}Cu_2N_6O_{12}$	$C_{14}H_{24}Cu_2N_6O_{12}$
M (g mol^{-1})	595.47	595.47
λ (Å)	0.6889	0.6889
Crystal system	trigonal	trigonal
Space group	$P3_1\,21$	$P3_1\,21$
a (Å)	10.802(4)	10.790(4)
c (Å)	16.933(6)	16.891(7)
V (Å^3)	1710.9(14)	1703.0(15)
Z	3	3
ρ_{calc} (g cm^{-3})	1.734	1.742
μ (mm^{-1})	1.785	1.793
T (K)	150(2)	260
θ range for data collection (°)	2.411- 30.396	2.113- 30.384
Completeness to θ = 25.0	100%	100%
Measured reflections	19288	19373
Unique reflections	3642	3647
Observed reflections [$I > 2\sigma(I)$]	2543	2508
Goof	1.031	1.031
Absolute structure parameter (Flack)	0.00 (1)	0.02(2)
R^a [$I > 2\sigma(I)$] (all data)	0.0557 (0.0813)	0.0496 (0.0763)
wR^b [$I > 2\sigma(I)$] (all data)	0.1617 (0.1798)	0.1355 (0.1511)
CCDC	1891588	1891589

^{a} $R = \sum(|F_o| - |F_c|)/\sum|F_o|$. ^{b} $wR = [\sum w(|F_o| - |F_c|)^2/\sum w|F_o|^2]^{1/2}$.

Table S5. Summary of Crystallographic Data for N_2@1, CO_2@1, Ar@1 and C_3H_6@1.

Compound	**N_2@1 (110 K/7.4 bar)**	**N_2@1 (226 K/7.5 bar)[c]**	**CO_2@1 (235 K/9.4 bar)**	**CO_2@1 (298 K/9.4 bar)**	**Ar@1 (120 K/10 bar)**	**Ar@1 (160 K/10 bar)**	**C_3H_6@1 (290 K/7.5 bar)**	**C_3H_6@1 (230 K/1 bar)**
Formula	$C_{14}H_{12}Cu_2N_{18}O_6$	$C_{14}H_{12}Cu_2N_{18}O_6$	$C_{17}H_{12}Cu_2N_6O_{12}$	$C_{17}H_{12}Cu_2N_6O_{12}$	$C_{14}H_{12}Cu_2N_{18}O_6$ $Ar_{0.67}$	$C_{14}H_{12}Cu_2N_{18}O_6$ $Ar_{0.67}$	$C_{20}H_{24}Cu_2N_6O_6$	$C_{26}H_{24}Cu_2N_6O_6$
M (g mol^{-1})	655.50	655.50	619.41	619.41	514.01	514.01	571.53	571.53
λ (Å)	0.6889	0.6889	0.6889	0.6889	0.6889	0.6889	0.6889	0.6889
Crystal system	trigonal	trigonal	trigonal	trigonal	trigonal	trigonal	trigonal	trigonal
Space group	$P3_121$	$P3_121$	$P3_121$	$P3_121$	$P3_121$	$P3_121$	$P3_121$	$P3_121$
a (Å)	10.324(4)	10.5951(12)	10.564(4)	10.7877(17)	10.134(3)	10.175(3)	10.709(4)	10.476(12)
c (Å)	16.712(8)	16.8331(15)	16.921(6)	17.088(3)	16.514(4)	16.621(6)	16.881(7)	16.66(2)
V (Å^3)	1542.7(14)	1636.5(4)	1635.4(13)	1722.2(6)	1468.8(8)	1490.1(11)	1676.8(13)	1584(4)
Z	3	3	3	3	3	3	3	3
ρ_{calc} (g cm^{-3})	2.117	1.995	1.887	1.792	1.743	1.71	1.698	1.798
μ (mm^{-1})	1.899	1.791	1.793	1.702	2.066	2.036	1.729	1.831
T (K)	110	226	235	298	120	160	230	290
θ range for data collection (°)	2.208 - 24.986		2.158 - 30.362	2.113 - 24.986	2.249 - 30.411	2.536 - 24.987	2.128- 24.981	2.176 - 24.415
Completeness to θ = 25.0	100%		100%	100 %	100%	100 %	100 %	78 %
Measured reflections	7377	2796	19074	15762	19503	7268	7231	5091
Unique reflections	1975	2440	3314	2207	3167	1892	2081	1406
Observed reflections [$I > 2\sigma(I)$]	1650	1919	2130	1837	2267	1565	1349	791
Goof	1.220		1.000	1.048	1.049	1.037	1.054	1.088
Absolute structure parameter (Flack)	0.03(5)		0.01(2)	-0.01(2)	0.00(2)	-0.016(18)	0.06(4)	0.01(5)
R^a [$I > 2\sigma(I)$] (all data)	0.1527 (0.1661)		0.0596 (0.0929)	0.0736 (0.0830)	0.0635 (0.0879)	0.0517 (0.0625)	0.1091 (0.1328)	0.1305 (0.1664)
wR^b [$I > 2\sigma(I)$] (all data)	0.3275 (0.3571)		0.1561 (0.1742)	0.2073 (0.2194)	0.1587 (0.1740)	0.1363 (0.1435)	0.2655 (0.2903)	0.2940 (0.3281)
CCDC	1891590		1891591	1891592	1891593	1891594	1891595	1891596

$^a R = \sum(|F_o| - |F_c|)/\sum|F_o|$. ^{b} $wR = [\sum w(|F_o| - |F_c|)^2/\sum w|F_o|^2]^{1/2}$.

[c]Refinement of data collected at 226 K, even if at high pressure, revealed no significant peaks of electron density attributable to guests in the channels, thus only data collection parameters have been reported.

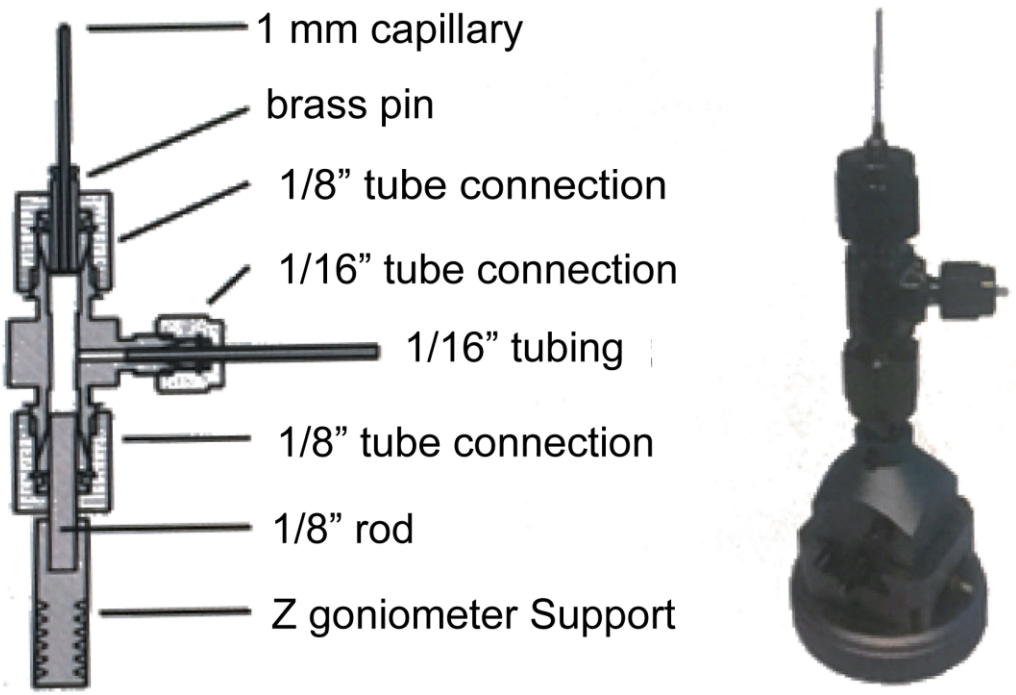

Vacuum - 10^{-5} mbar
Maximum pressure - 150 bar
Number of cells: 8

Figure S1. (a) Diagram of a capillary dosing assembly. (b) Capillary static cell designed and built at Diamond Light Source Beamline I19.

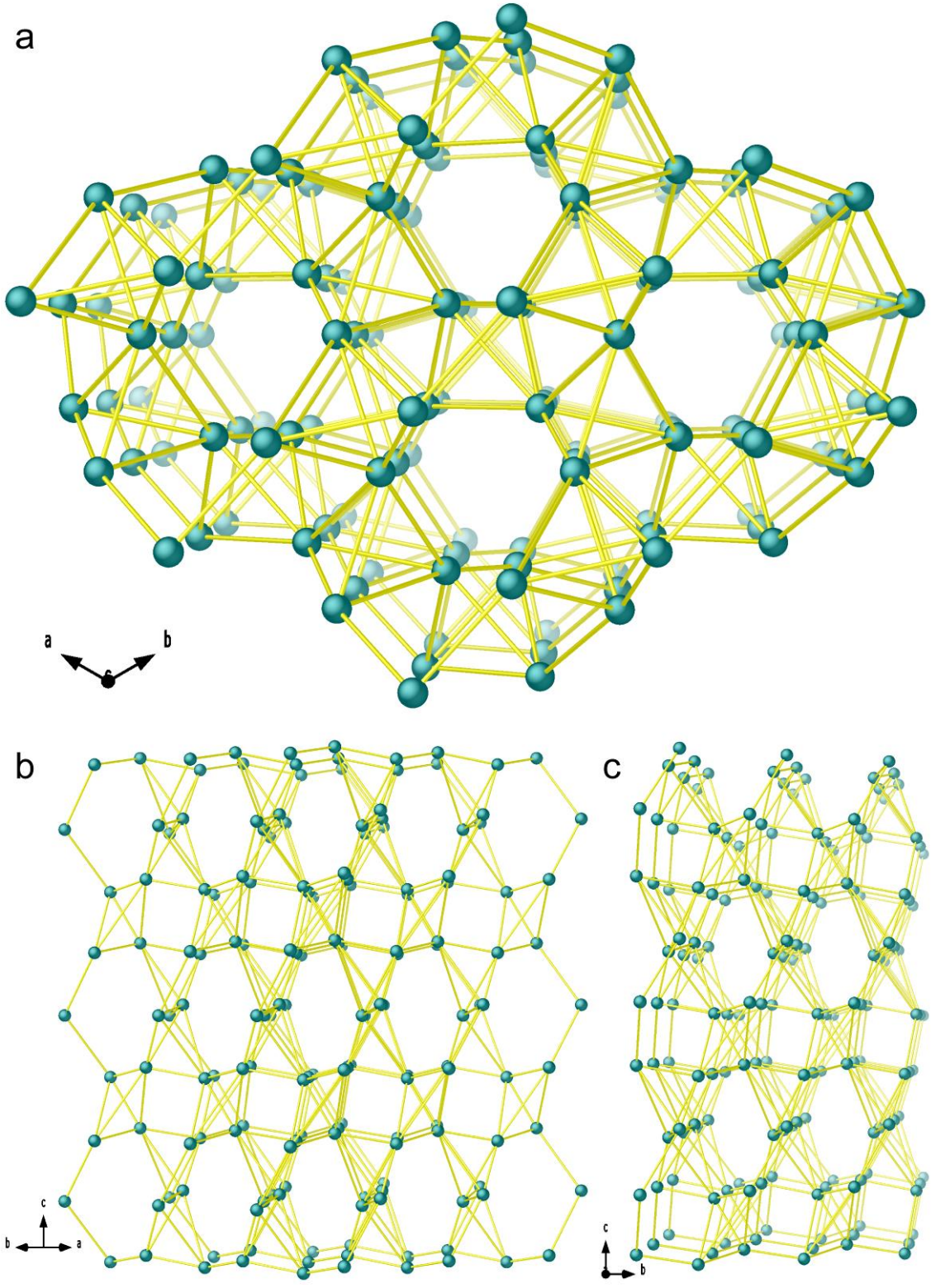

Figure S2. (a) Perspective view along *c* crystallographic axis of the 3D underlying uninodal 6-connected net with stoichiometry (6-c) and point symbol for net $\{3^6.6^3.7^5.8\}$. Perspective views along the [110] (b) and [100] directions (c) emphasizing the **qtz-e**-type topology of **1**.

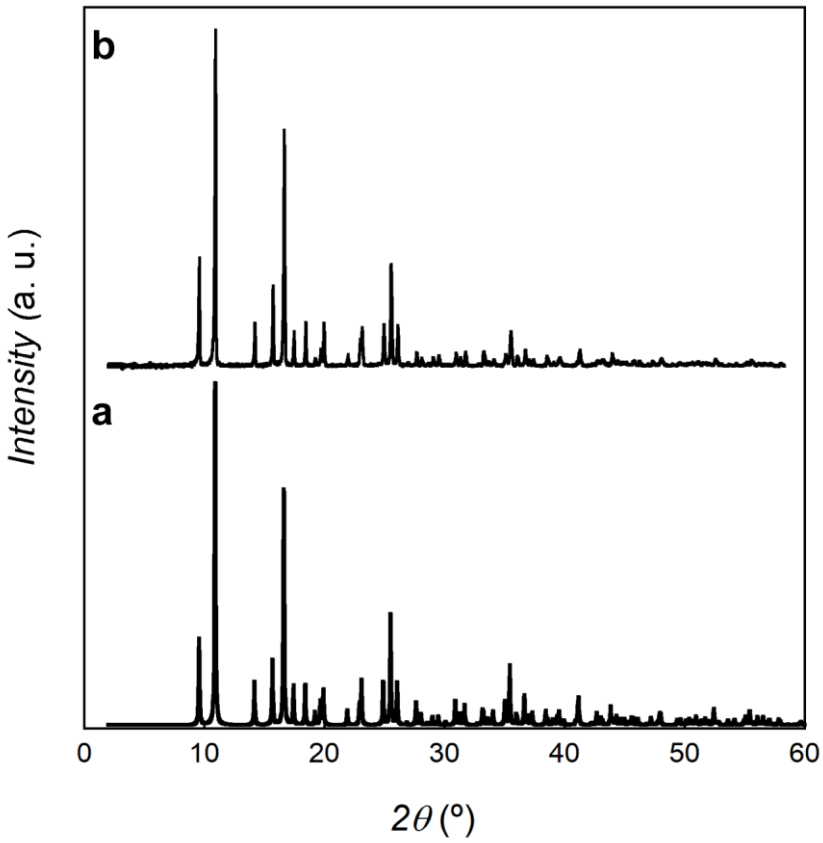

Figure S3. Calculated (a) and experimental (b) PXRD pattern profiles of **1** in the 2θ range 2–60° at RT.

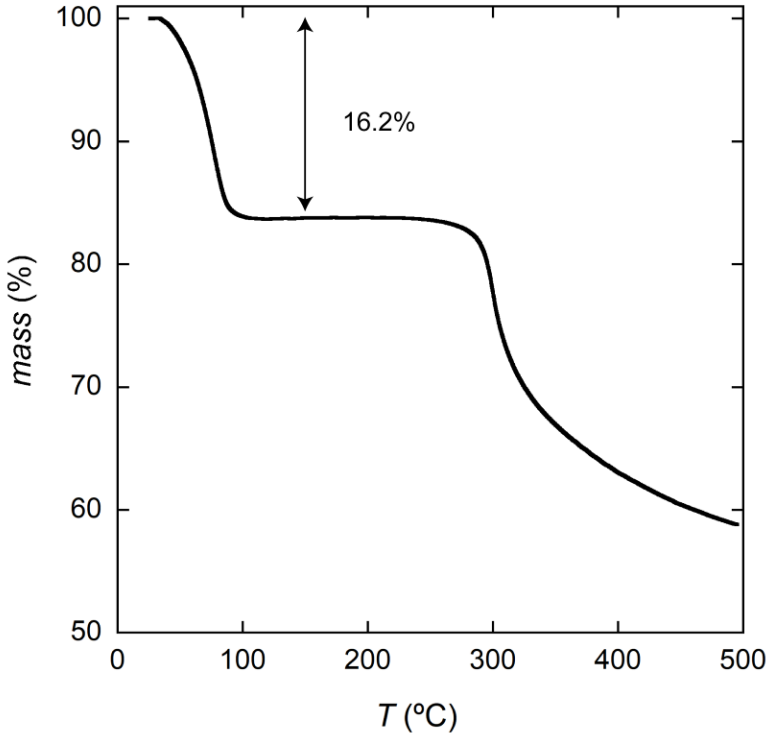

Figure S4. Thermo-Gravimetric Analyses (TGA) of **1**, in the 25-500 ºC range, under a dry N_2 atmosphere.

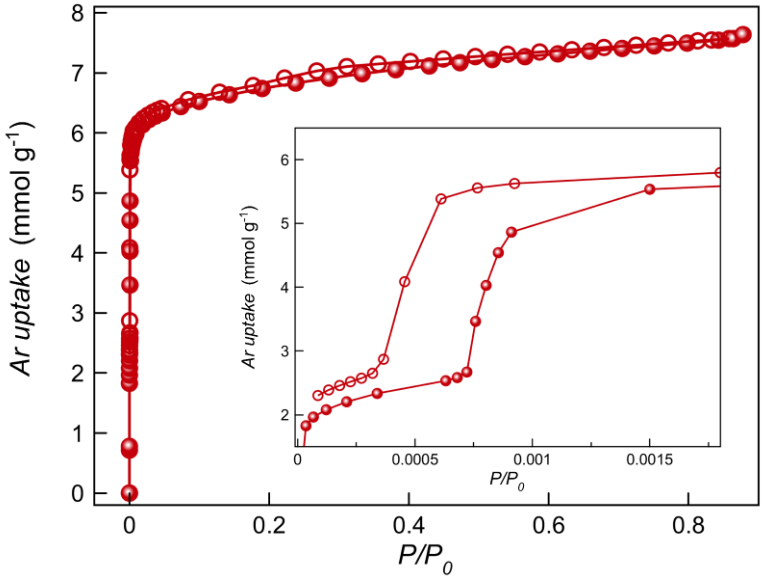

Figure S5. Ar (77 K) adsorption isotherm for the activated compound **1**. Filled and empty symbols indicate the adsorption and desorption isotherms, respectively. The inset shows the two-step gas adsorption and the hysteresis in the desorption process at low pressures.

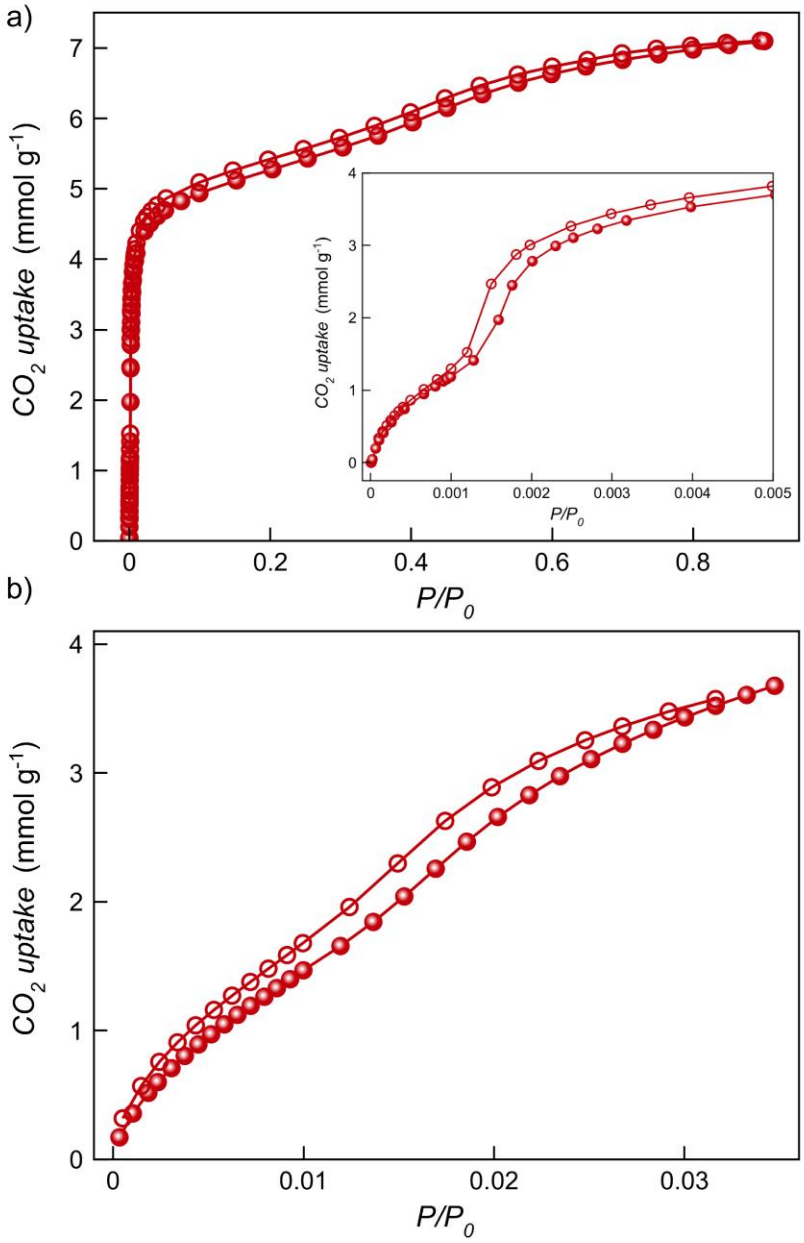

Figure S6. CO_2 adsorption isotherms at 195 K (a) and 273 K (b) for the activated compound **1**. Filled and empty symbols indicate the adsorption and desorption isotherms, respectively. The inset in S6a shows the two-step gas adsorption and the hysteresis in the desorption process at low pressures.

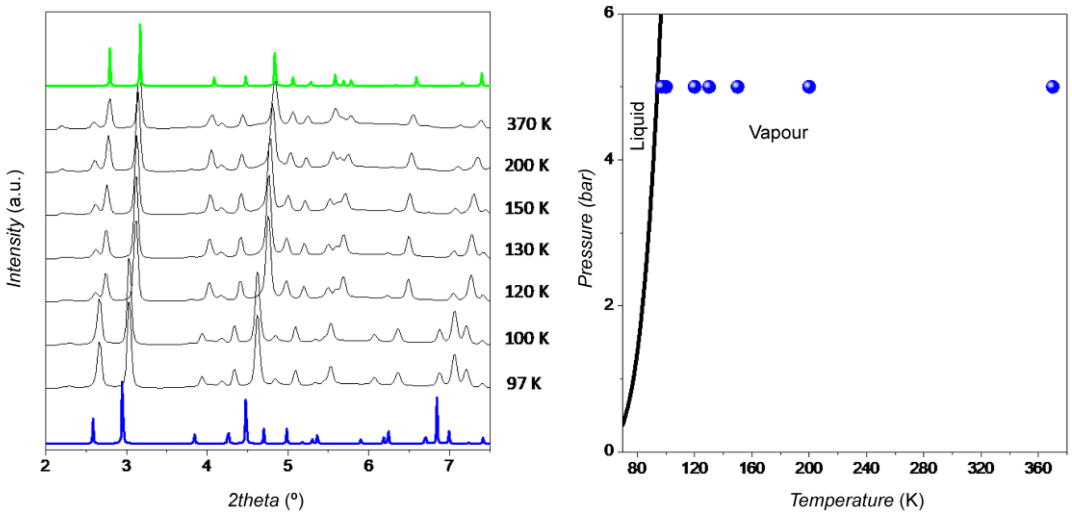

Figure S7. (a) This graph shows the S-PXRD of compound **1** pressurized with 5 bar of N_2 and different temperatures (black), pattern of simulated hydrated phase (blue), simulated pattern of the dehydrated phase (green). (b) represent the phase diagram of N_2 and the blue circle shows where the S-PXRD are taken.

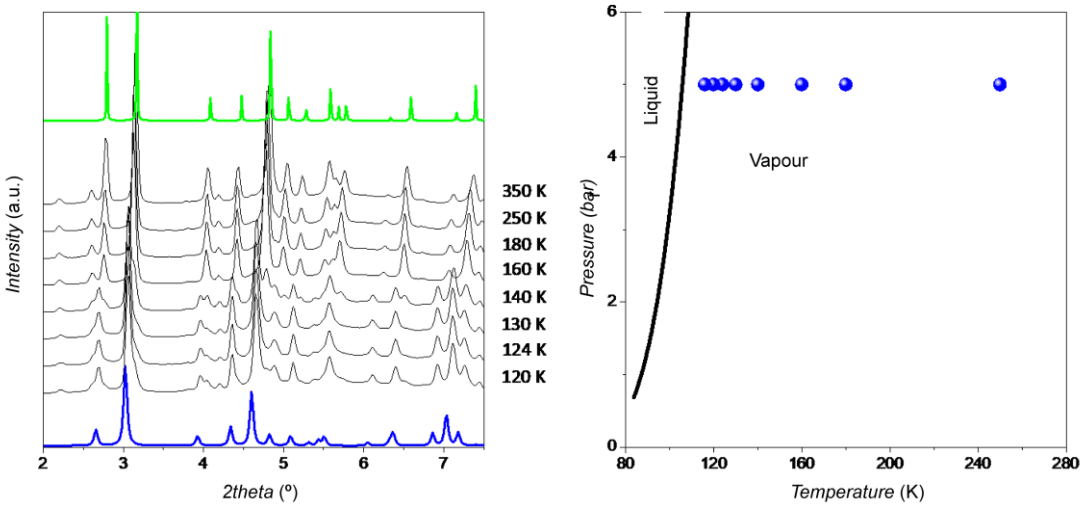

Figure S8. (a) This graph shows the S-PXRD of compound **1** pressurized with 5 bar of Ar and different temperatures (black), pattern of simulated hydrated phase (blue), simulated pattern of the dehydrated phase (green). (b) represent the phase diagram of Ar and the blue circle shows where the S-PXRD are taken.

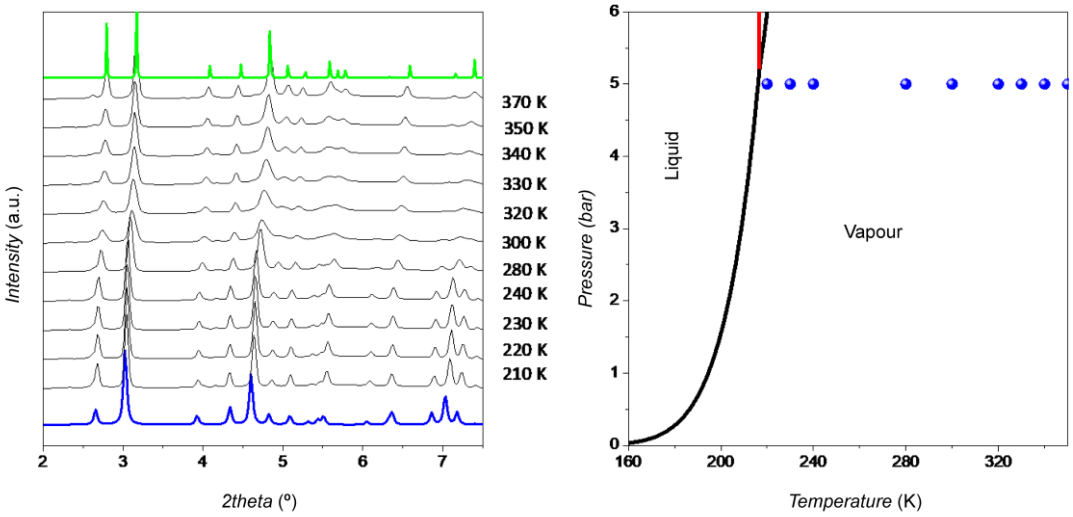

Figure S9. (a) This graph shows the S-PXRD of compound **1** pressurized with 5 bar of CO_2 and different temperatures (black), pattern of simulated hydrated phase (blue), simulated pattern of the dehydrated phase (green). (b) represent the phase diagram of CO_2 and the blue circle shows where the S-PXRD are taken.

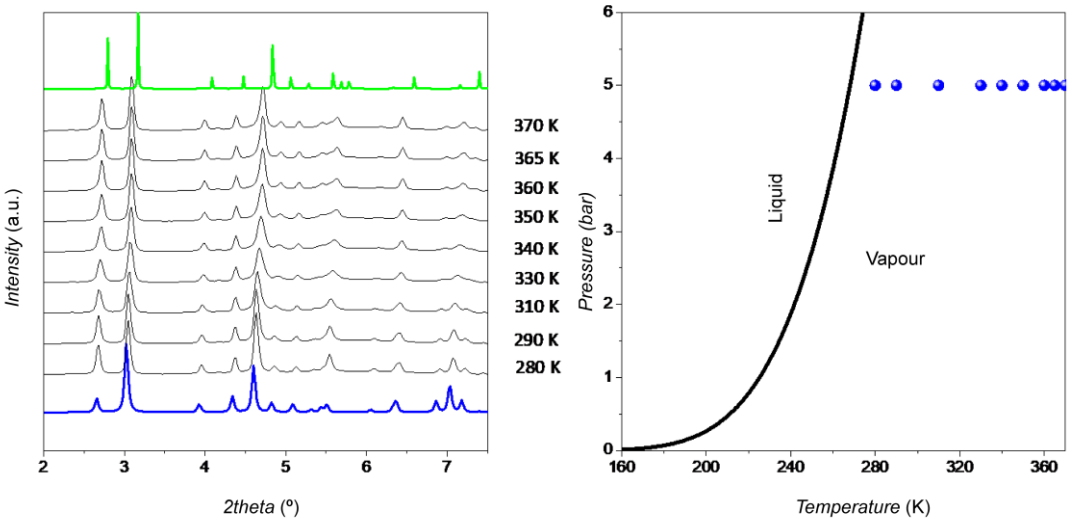

Figure S10. (a) This graph shows the S-PXRD of compound **1** pressurized with 5 bar of propene (C_3H_6) and different temperatures (black), pattern of simulated hydrated phase (blue), simulated pattern of the dehydrated phase (green). (b) represent the phase diagram of propene and the blue circle shows where the S-PXRD are taken.

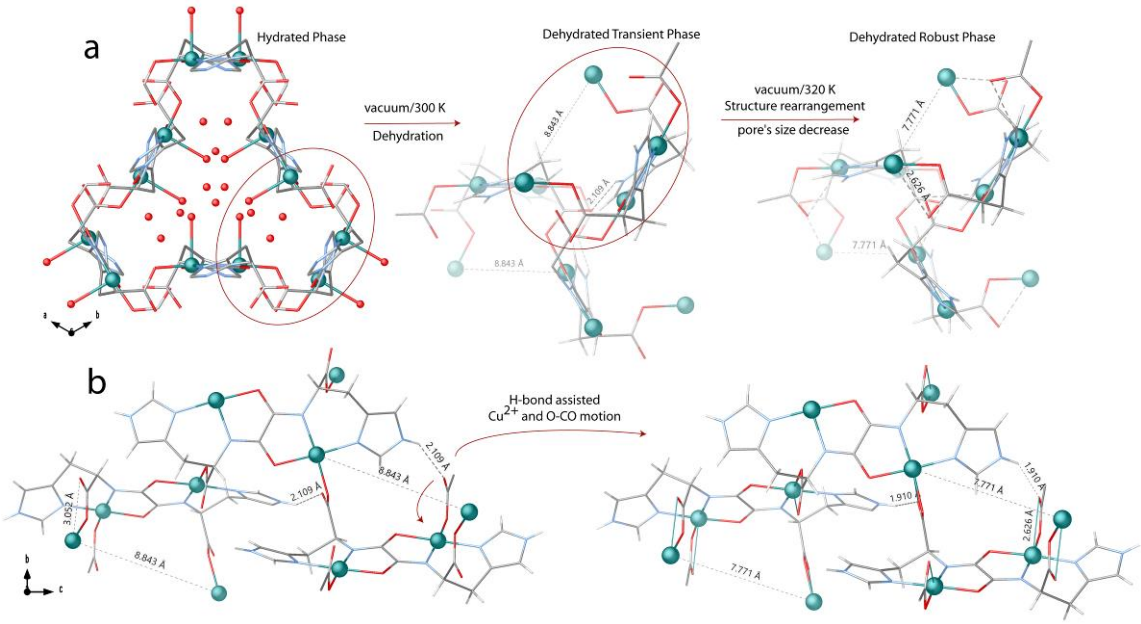

Figure S11. Crystal structures of hydrated, transient dehydrated and robust dehydrated phases of **1** (a). View along the *c* axis of one pore's details of the 3D open-framework from original structure of **1** (at 293 K) through steps for *transient* and robust dehydrated phase. (b) Details of one pore viewed along the *a* axis for *transient* (left) and robust hydrated phase (right). The guest water molecules are represented as red spheres. The main structural variations are shown in detail (dashed lines). Color codes: Cu: cyan; O: red; C: gray; N: blue.

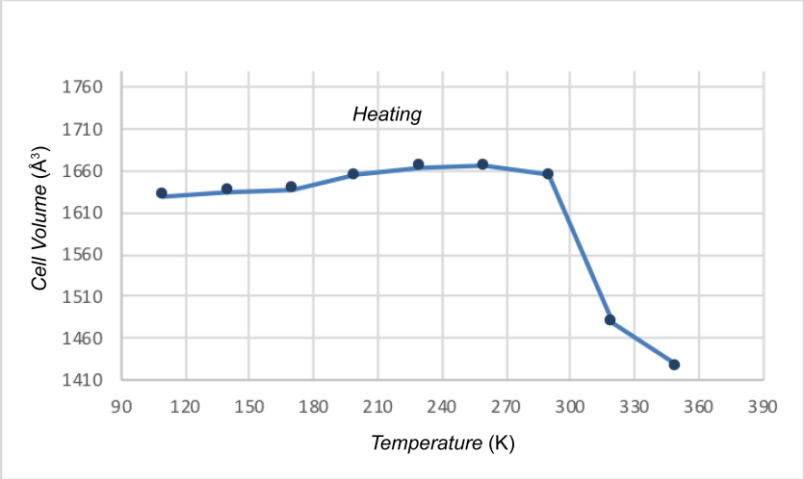

Figure S12. Cell volume changes of crystal structures of **1** during heating.

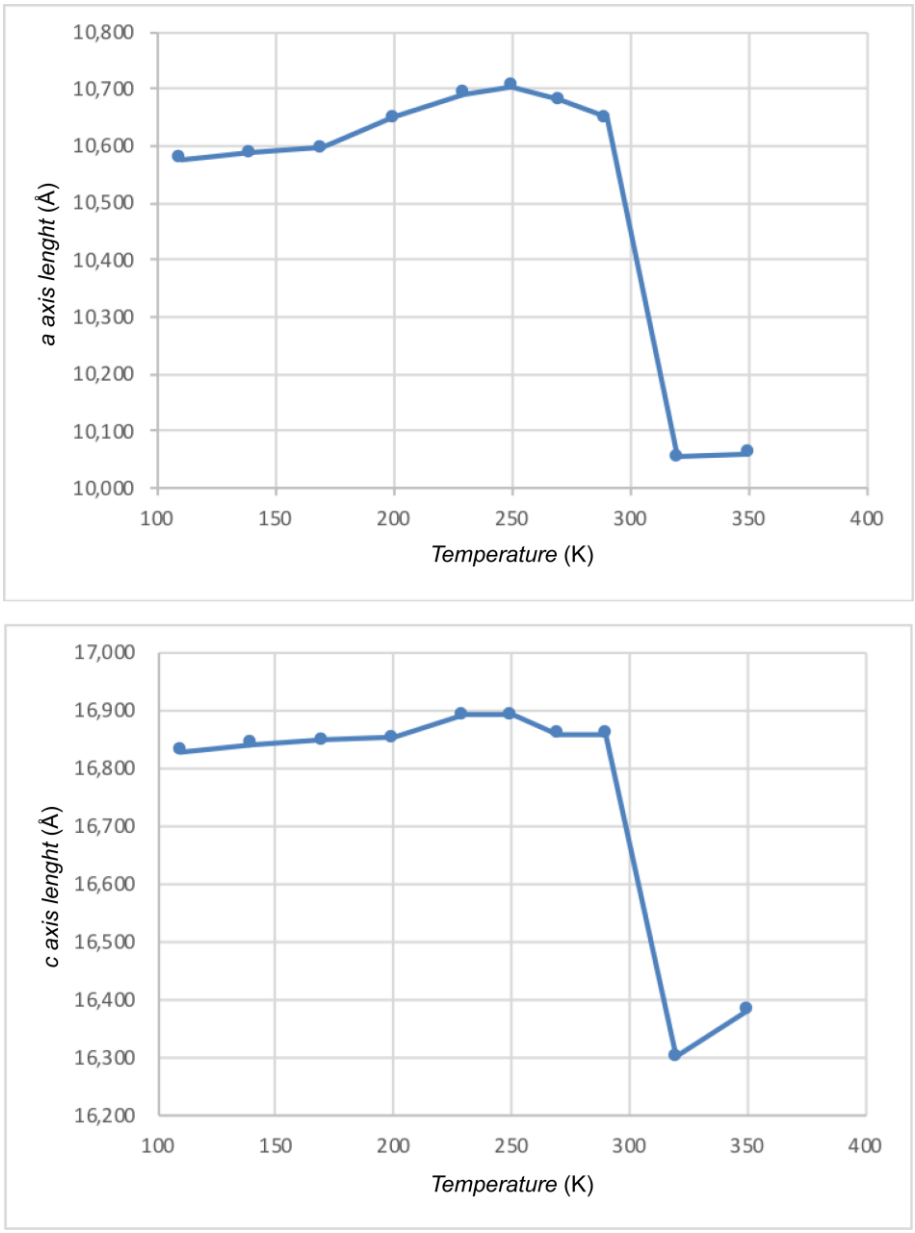

Figure S13. Changes to the *a*- (top) and *c*- (bottom) axis lengths, registered by SCXRD, of **1** during solvent removal.

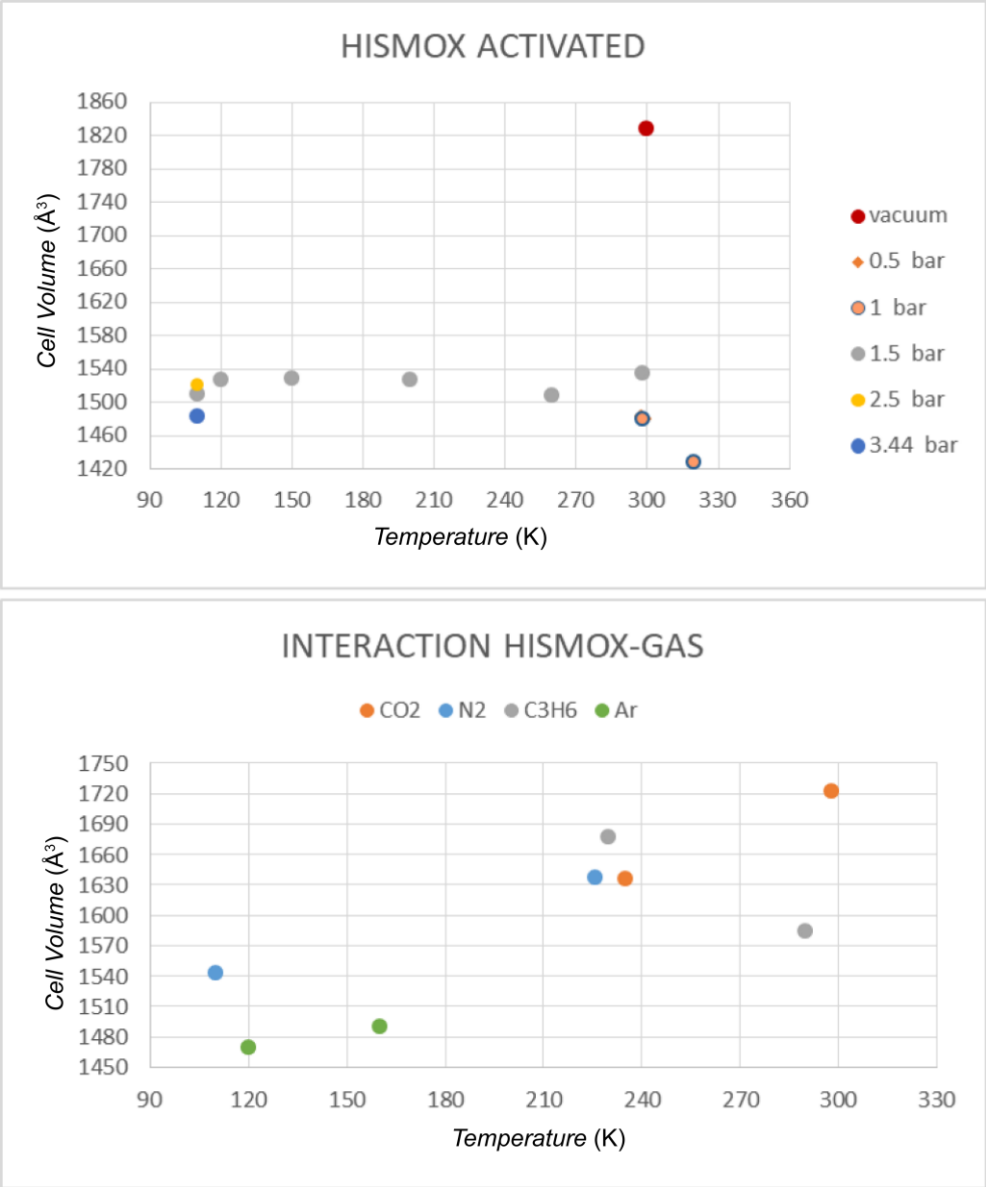

Figure S14. Cell volume changes registered by SCXRD of activated crystal structures of **1** (top) and under pressure of different gases (N_2, Ar, CO_2 and C_3H_6) (bottom) at different temperatures.

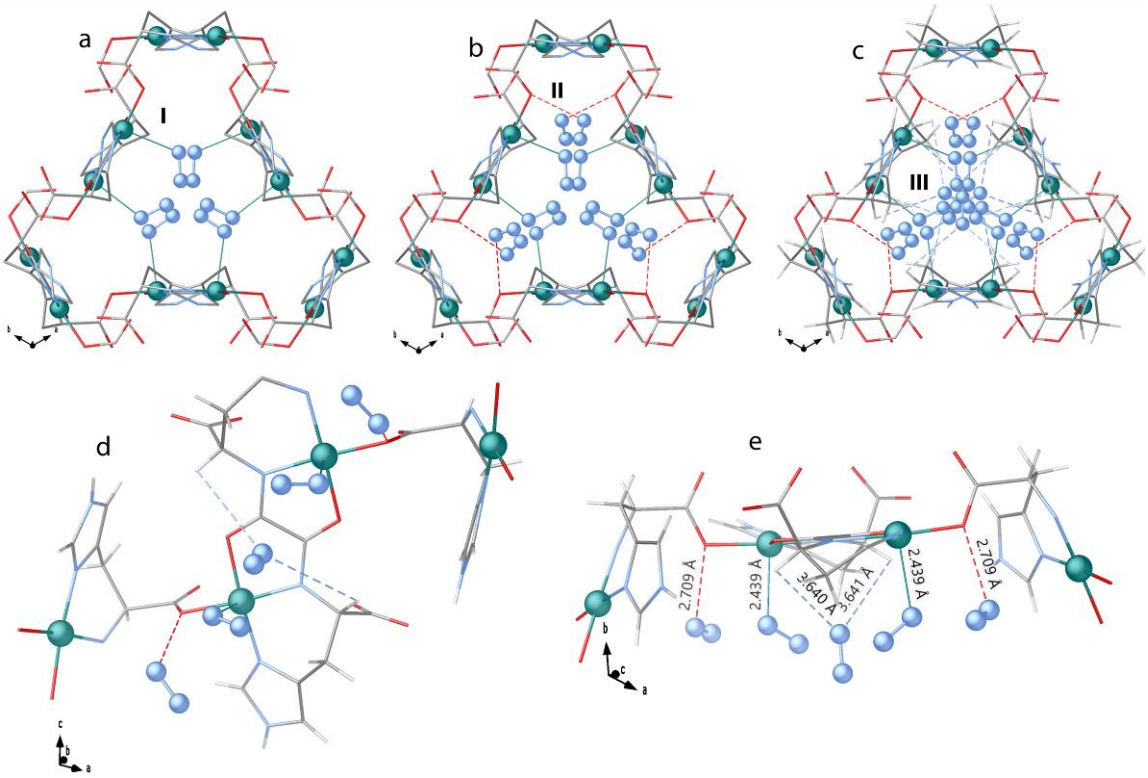

Figure S15. A portion of the crystal structures of **N_2@1** (110 K, 7.4 bar) along the *c* axis underlining the three diverse adsorption sites (a-c) I (green lines in a), II (red dashed lines in b) and III (sky blue dashed lines in c) and side views (d-e) showing details and structural parameters related to N_2 guest molecule interactions. The ligands are depicted as sticks and the copper(II) cations together with N_2 guests as spheres. Color codes: Cu: cyan; O: red; C: gray; N: blue.

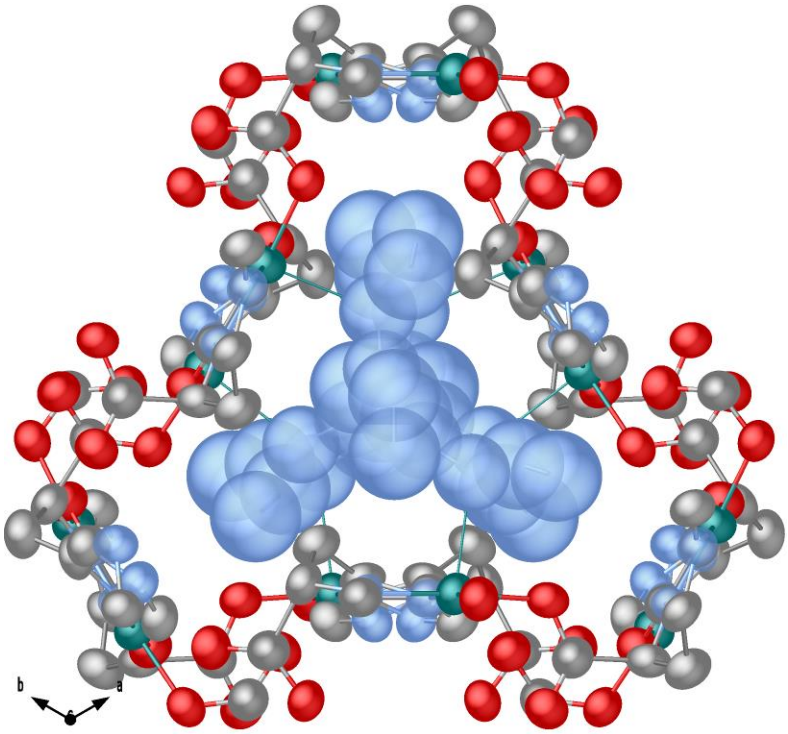

Figure S16. Detailed view of one single channel of **N_2@1** (110 K, 7.4 bar) along the *c* axis showing thermal ellipsoids at 50% of probability levels. Hydrogen atoms are omitted for clarity. Color codes: Cu: cyan; O: red; C: gray; N: blue.

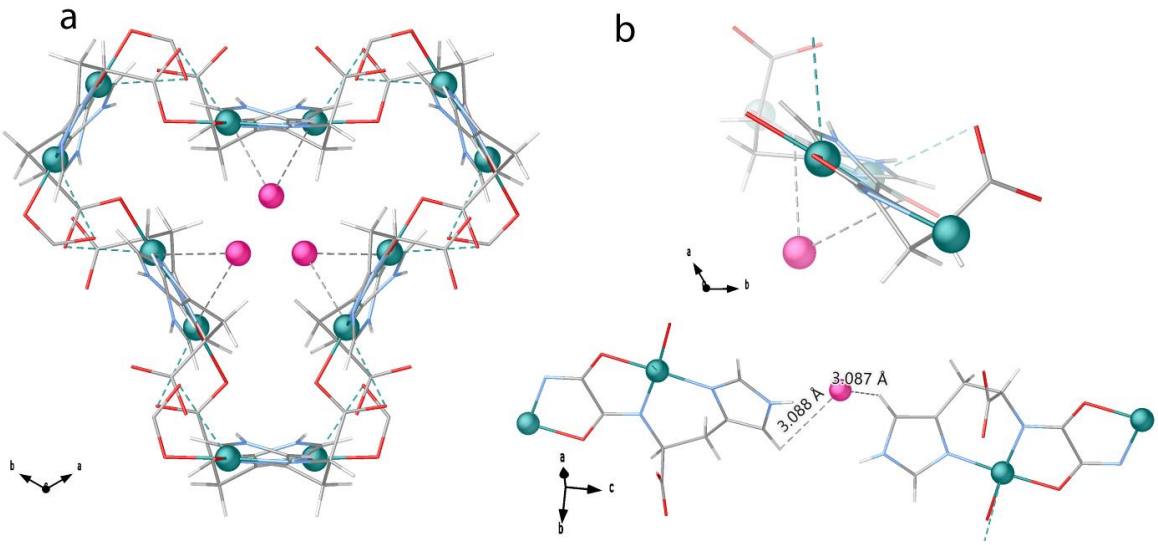

Figure S17. A portion of the crystal structures of **Ar@1**. Detailed view of one single channel of **Ar@1** (120 K, 10 bar) along the *c* axis (a) and side view details (b). of the adsorption site (grey dashed lines). The ligands are depicted as sticks and the copper(II) cations together with Ar guests as spheres. Color codes: Cu: cyan; Ar: purple; O: red; C: gray; N: blue.

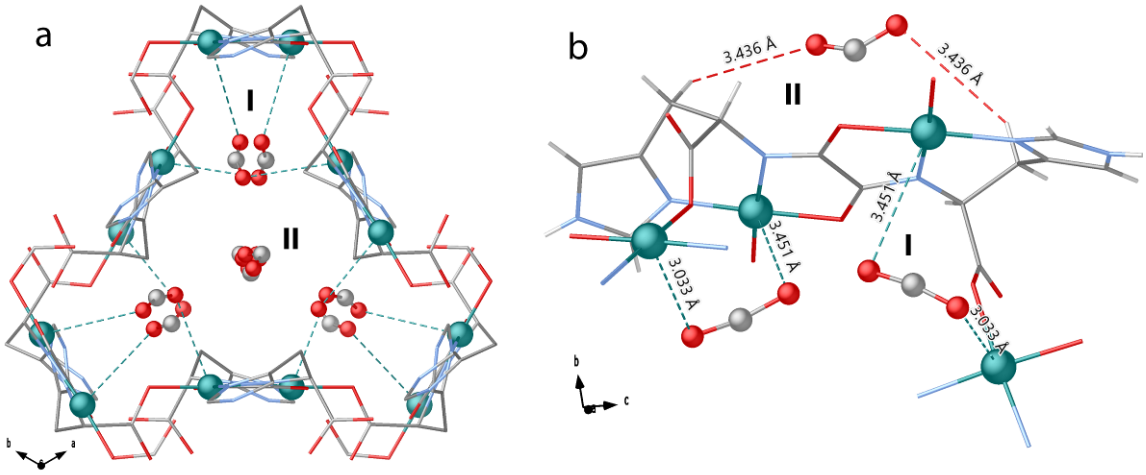

Figure S18. A portion of the crystal structures of **CO_2@1**. Detailed view of one single channel of **CO_2@1** (235 K, 9.4 bar) along the *c* axis (a) and side view details (b). of the two diverse adsorption sites I (cyan dashed lines) and II (red dashed lines). The ligands are depicted as sticks and the copper(II) cations together with CO_2 guests as spheres. Hydrogen atoms in a are omitted for clarity. Color codes: Cu: cyan; O: red; C: gray; N: blue.

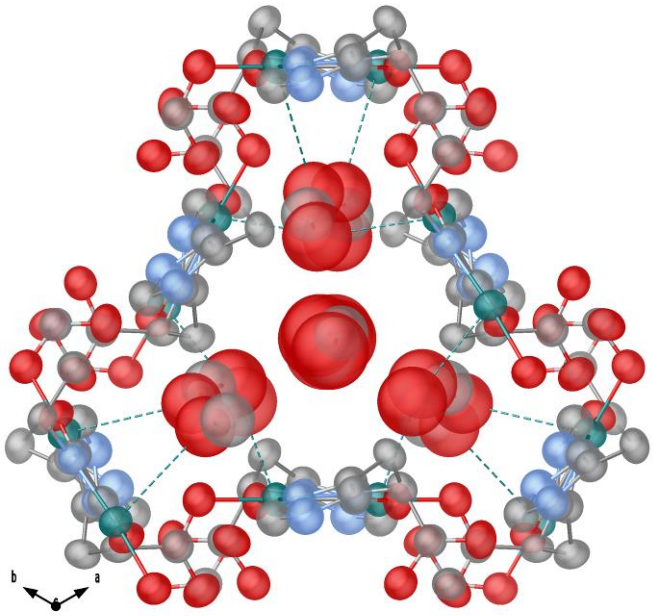

Figure S19. Detailed view of one single channel of **CO_2@1** (235 K, 9.4 bar) along the *c* axis showing thermal ellipsoids at 50% of probability levels. Hydrogen atoms are omitted for clarity. Color codes: Cu: cyan; O: red; C: gray; N: blue.

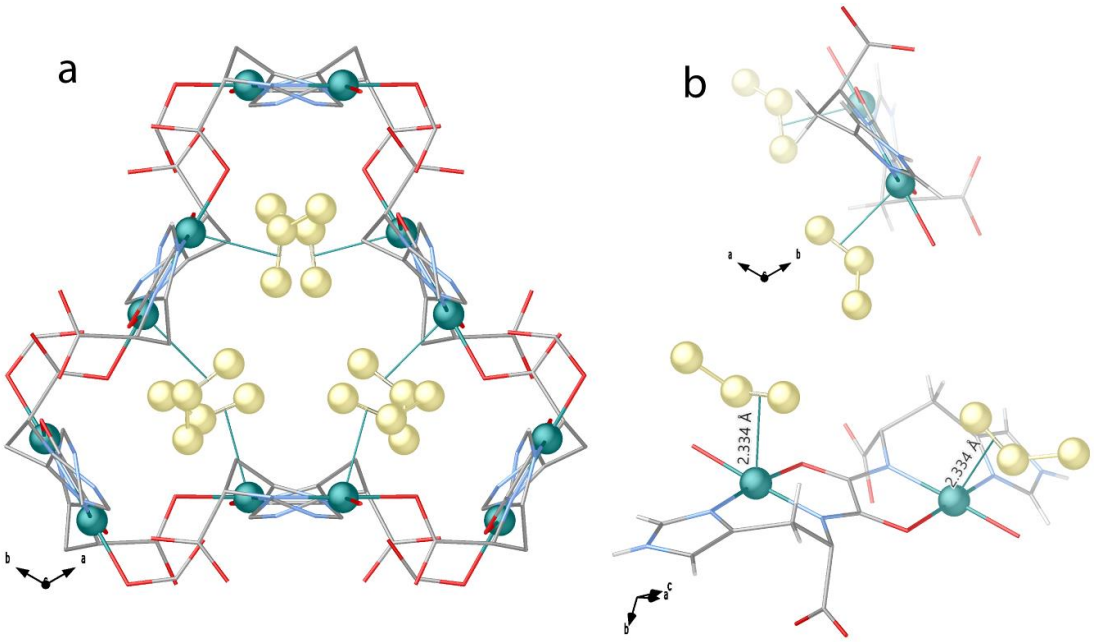

Figure S20. A portion of the crystal structures of **C_3H_6@1** (290 K, 7.5 bar). Detailed view of one single channel along the *c* axis (a) and side view details (b) of the adsorption site (cyan dashed lines) The ligands are depicted as sticks and the copper(II) cations together with C_3H_6 guests as spheres (depicted as yellow spheres). Hydrogen atoms in a are omitted for clarity. Color codes: Cu: cyan; O: red; C: gray; N: blue.

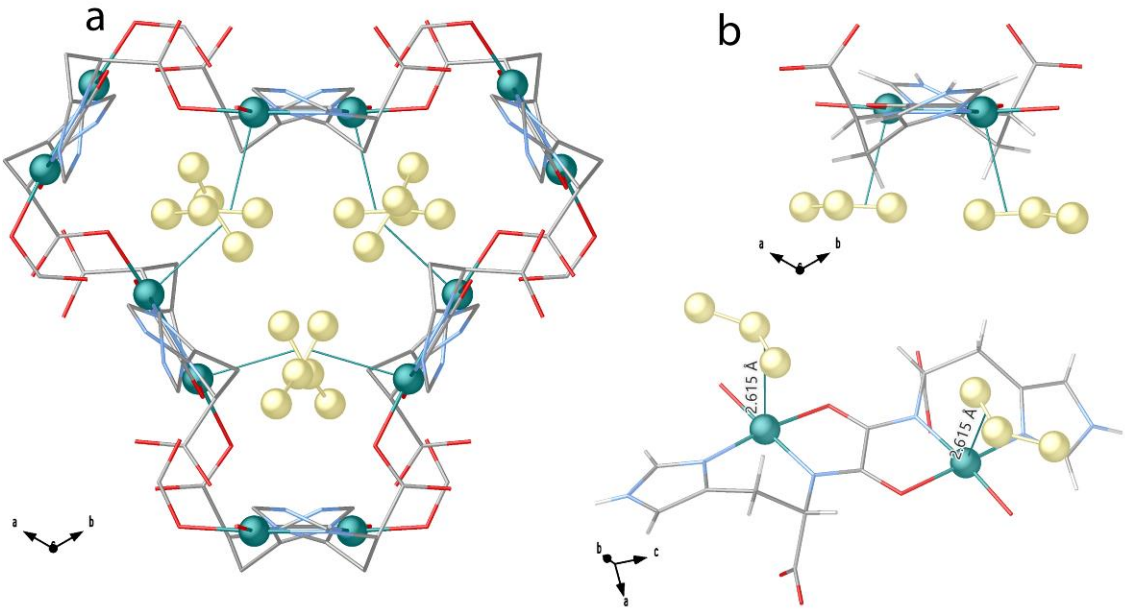

Figure S21. A portion of the crystal structures of **C_3H_6@1** (230 K, 1 bar). Detailed view of one single channel along the *c* axis (a) and side view details (b) of the adsorption site (cyan dashed lines) The ligands are depicted as sticks and the copper(II) cations together with C_3H_6 guests as spheres (depicted as yellow spheres). Hydrogen atoms in a are omitted for clarity. Color codes: Cu: cyan; O: red; C: gray; N: blue.

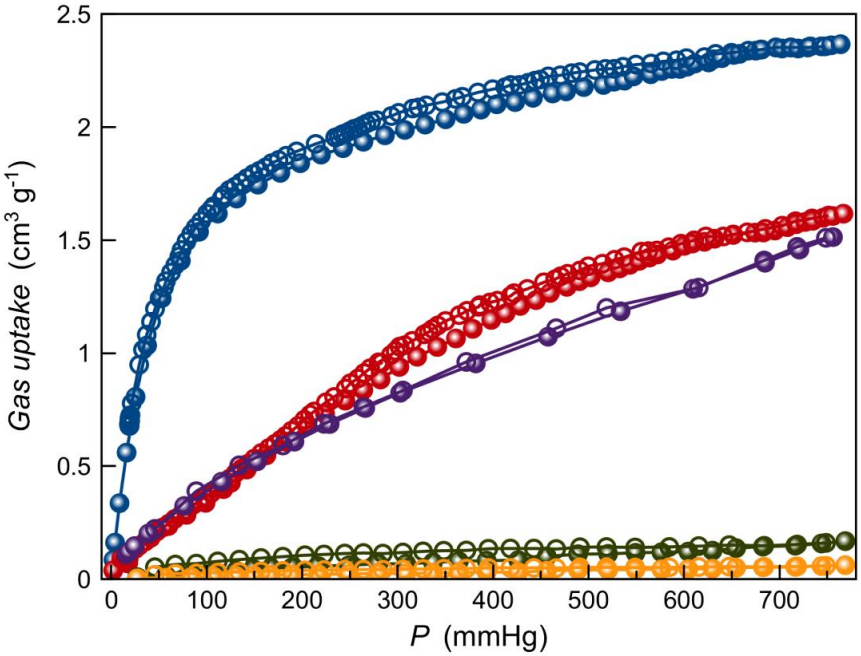

Figure S22. C_3H_6 (blue), C_3H_8 (red), CO_2 (purple), CH_4 (green) and N_2 (orange) adsorption isotherms at 298 K for the activated compound **1**. Filled and empty symbols indicate the adsorption and desorption isotherms, respectively.

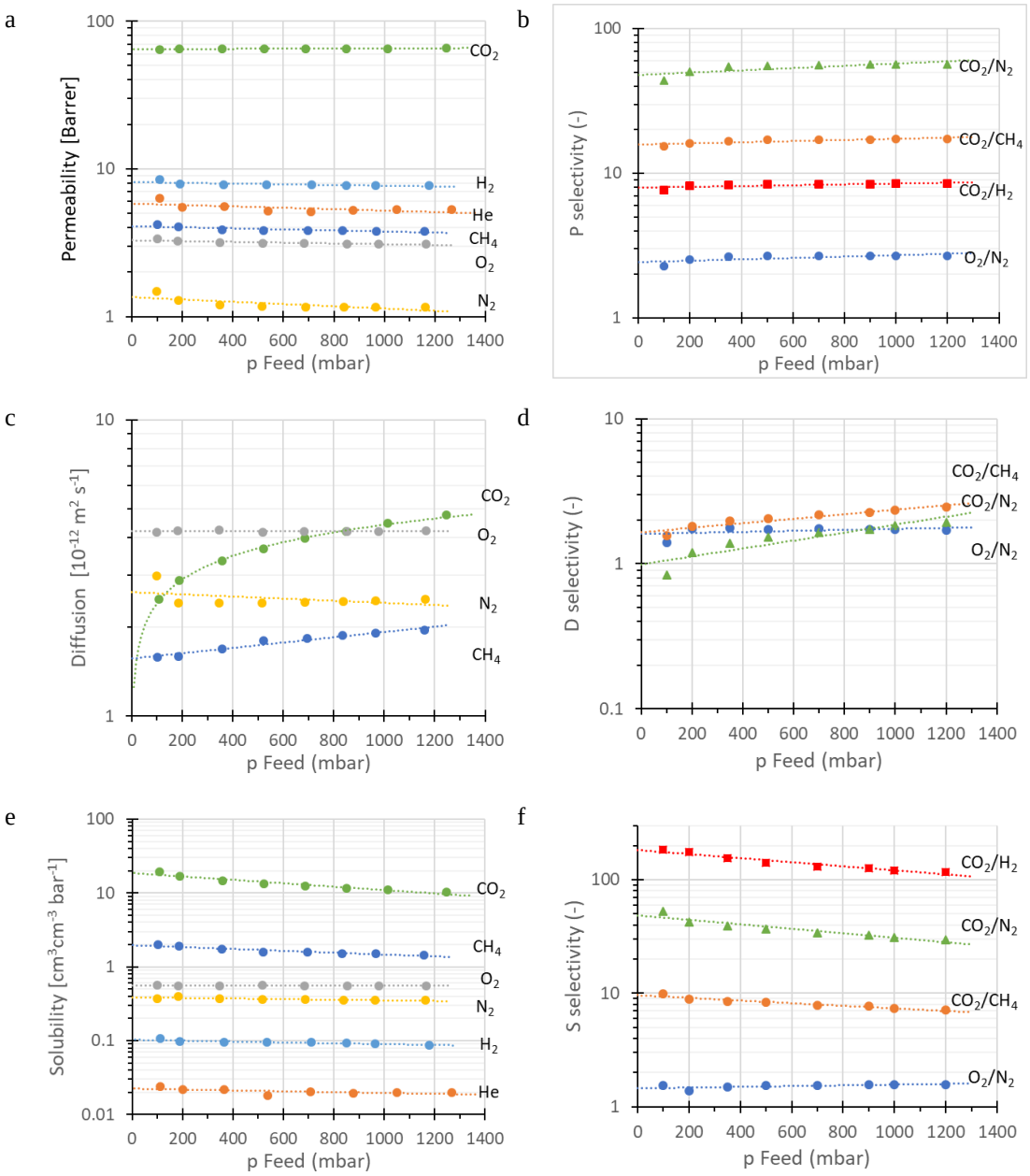

Figure S23. Feed pressure dependence of (a) permeability, (c) diffusion, (e) solubility and b) permselectivity, (d) diffusion selectivity and (f) solubility selectivity in membrane Pebax1657 + 22 vol%**1**. Lines are indicated as a guide to the eye.

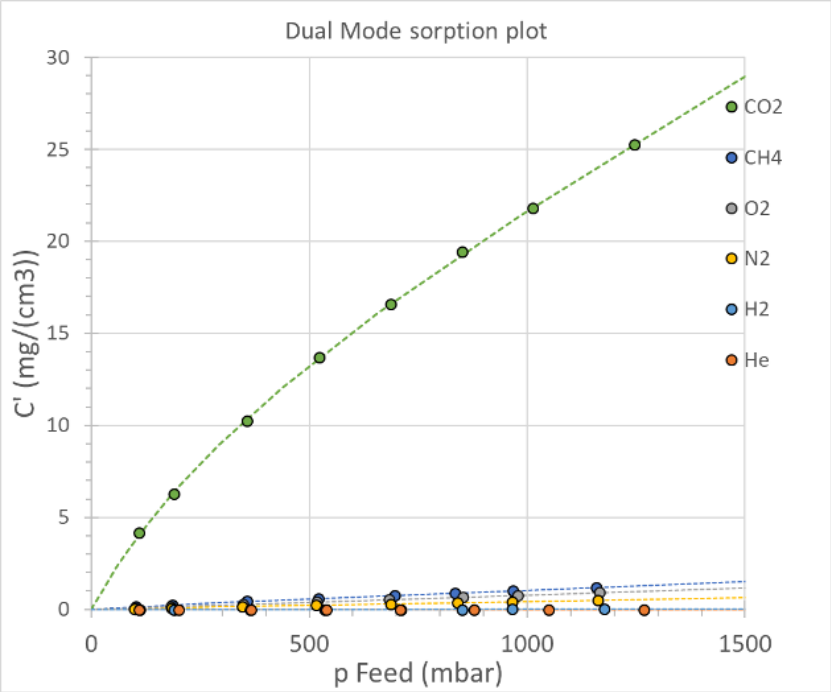

Figure S24. Sorption isotherms as determined by the pressure-increase method for six gases in the Pebax1657+22 vol%**1** membrane

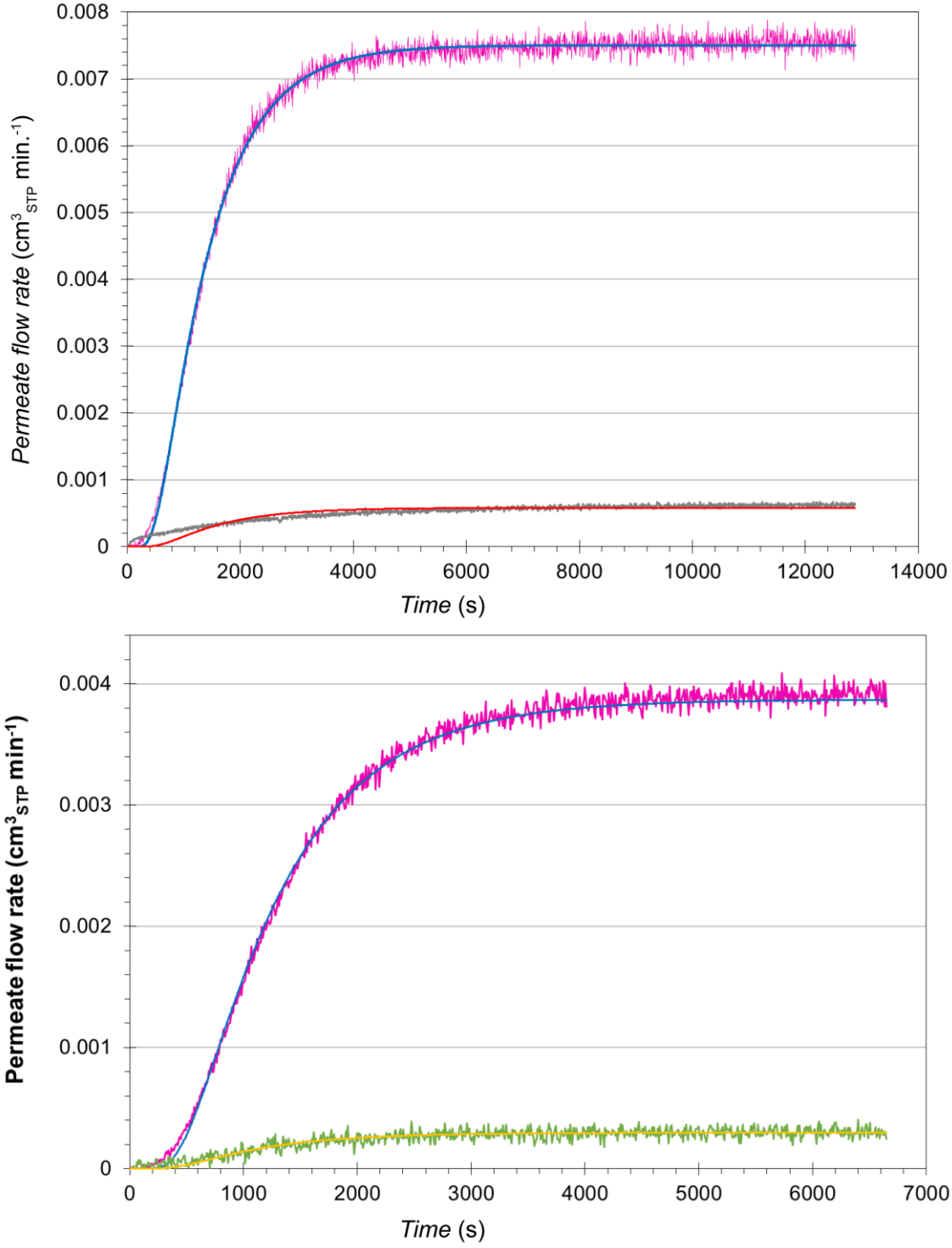

Figure S25. Sigmoidal curve of the permeate flow rate for MMMs based on Pebax1657/amine-derived-MOF1 using (a) the binary mixture CO_2/CH_4 (35/65 v/v) and (b) the binary mixture CO_2/N_2 (15/85 v/v), (pink curve for CO_2, grey curve for CH_4, and green curve for N_2).

REFERENCES

(1) Mon, M.; Ferrando-Soria, J.; Verdaguer, M.; Train, C.; Paillard, C.; Dkhil, B.; Versace, C.; Bruno, R.; Armentano, D.; Pardo, E. *J. Am. Chem. Soc.* **2017**, *139* (24), 8098.

(2) (a) Evans, P. *Acta Cryst.* **2006**, D62, 72-82; (b) Evans, P. R. and Murshudov, G. N. *Acta Cryst.* **2013**, D69, 1204-1214; (c) Winn, M. D. et al. *Acta Cryst.* **2011**, D67, 235-242; (d) Winter, G. *J. Appl. Cryst.*, **2010**, *43*, 186-190; € Winter, G. et al. *Acta Cryst.* **2018**, D74, 85-97.

(3) (a) Sheldrick G.M. *J. Appl.Cryst.* **2015**, *48*, 3-10; (b) G. M. Sheldrick, *Acta Cryst.*, **2015**, A71 3-8. (c) G. M. Sheldrick, *Acta Cryst.* **2008**, *A64*, 112-122.

(4) Zhang, J.-P.; Chen, X.-M. *J. Am. Chem. Soc.* **2008**, *130* (18), 6010.

(5) Vaidhyanathan, R.; Iremonger, S. S.; Shimizu, G. K. H.; Boyd, P. G.; Alavi, S.; Woo, T. K. *Science.* **2010**, *330* (6004), 650.

(6) Gonzalez, M. I.; Mason, J. A.; Bloch, E. D.; Teat, S. J.; Gagnon, K. J.; Morrison, G. Y.; Queen, W. L.; Long, J. R. *Chem. Sci.* **2017**, *8* (6), 4387.

(7) Jansen, J. C.; Friess, K.; Drioli, E. *J. Memb. Sci.* 2011, 367, 141–151, doi:10.1016/j.memsci.2010.10.063.

(8) Crank, J. The mathematics of diffusion; 2nd ed.; Clarendon Press: Oxford, 1975; ISBN 0198533446.

(9) Fraga, S. C.; Monteleone, M.; Lanč, M.; Esposito, E.; Fuoco, A.; Giorno, L.; Pilnáček, K.; Friess, K.; Carta, M.; McKeown, N. B.; Izák, P.; Petrusová, Z.; Crespo, J. G.; Brazinha, C.; Jansen, J. C. J. Memb. Sci. 2018, 561, 39–58, doi:10.1016/J.MEMSCI.2018.04.029.

(10) Monteleone, M.; Esposito, E.; Fuoco, A.; Lanč, M.; Pilnáček, K.; Friess, K.; Bezzu, C. G.; Carta, M.; McKeown, N. B.; Jansen, J. C. Membranes (Basel). 2018, 8, doi:10.3390/membranes8030073.